



# Scaling of precipitation extremes with temperature in the French Mediterranean region: What explains the hook shape?

Philippe Drobinski, Bastien Alonzo, Sophie Bastin, Nicolas Da Silva, Caroline Muller

## ► To cite this version:

Philippe Drobinski, Bastien Alonzo, Sophie Bastin, Nicolas Da Silva, Caroline Muller. Scaling of precipitation extremes with temperature in the French Mediterranean region: What explains the hook shape?. *Journal of Geophysical Research: Atmospheres*, American Geophysical Union, 2016, 121 (7), pp.3100-3119. <10.1002/2015JD023497>. <insu-01298539>

HAL Id: insu-01298539

<https://hal-insu.archives-ouvertes.fr/insu-01298539>

Submitted on 6 Apr 2016

**HAL** is a multi-disciplinary open access archive for the deposit and dissemination of scientific research documents, whether they are published or not. The documents may come from teaching and research institutions in France or abroad, or from public or private research centers.

L'archive ouverte pluridisciplinaire **HAL**, est destinée au dépôt et à la diffusion de documents scientifiques de niveau recherche, publiés ou non, émanant des établissements d'enseignement et de recherche français ou étrangers, des laboratoires publics ou privés.





## RESEARCH ARTICLE

10.1002/2015JD023497

## Key Points:

- Departures from the Clausius-Clapeyron thermodynamic expectation
- Impact of seasonal precipitation variability on precipitation extremes scaling
- Dynamical contribution of orography to precipitation extremes scaling

## Correspondence to:

P. Drobinski,  
philippe.drobinski@lmd.polytechnique.fr

## Citation:

Drobinski, P., B. Alonzo, S. Bastin, N. Da Silva, and C. Muller (2016), Scaling of precipitation extremes with temperature in the French Mediterranean region: What explains the hook shape?, *J. Geophys. Res. Atmos.*, 121, doi:10.1002/2015JD023497.

Received 23 APR 2015

Accepted 8 MAR 2016

Accepted article online 16 MAR 2016

## Scaling of precipitation extremes with temperature in the French Mediterranean region: What explains the hook shape?

**P. Drobinski<sup>1</sup>, B. Alonzo<sup>1,2</sup>, S. Bastin<sup>3</sup>, N. Da Silva<sup>1</sup>, and C. Muller<sup>2</sup>**

<sup>1</sup>LMD/IPSL, CNRS, Ecole Polytechnique, Université Paris-Saclay, Palaiseau, France, <sup>2</sup>LadHyX, CNRS, Ecole Polytechnique, Université Paris-Saclay, Palaiseau, France, <sup>3</sup>LATMOS/IPSL, CNRS, Université Versailles-Saint Quentin, Université Paris-Saclay, Guyancourt, France

**Abstract** Expected changes to future extreme precipitation remain a key uncertainty associated with anthropogenic climate change. Extreme precipitation has been proposed to scale with the precipitable water content in the atmosphere. Assuming constant relative humidity, this implies an increase of precipitation extremes at a rate of about 7% °C<sup>-1</sup> globally as indicated by the Clausius-Clapeyron relationship. Increases faster and slower than Clausius-Clapeyron have also been reported. In this work, we examine the scaling between precipitation extremes and temperature in the present climate using simulations and measurements from surface weather stations collected in the frame of the HyMeX and MED-CORDEX programs in Southern France. Of particular interest are departures from the Clausius-Clapeyron thermodynamic expectation, their spatial and temporal distribution, and their origin. Looking at the scaling of precipitation extreme with temperature, two regimes emerge which form a hook shape: one at low temperatures (cooler than around 15°C) with rates of increase close to the Clausius-Clapeyron rate and one at high temperatures (warmer than about 15°C) with sub-Clausius-Clapeyron rates and most often negative rates. On average, the region of focus does not seem to exhibit super Clausius-Clapeyron behavior except at some stations, in contrast to earlier studies. Many factors can contribute to departure from Clausius-Clapeyron scaling: time and spatial averaging, choice of scaling temperature (surface versus condensation level), and precipitation efficiency and vertical velocity in updrafts that are not necessarily constant with temperature. But most importantly, the dynamical contribution of orography to precipitation in the fall over this area during the so-called "Cevenoles" events, explains the hook shape of the scaling of precipitation extremes.

### 1. Introduction

Intensification of extreme hydrometeorological events by natural and anthropogenically forced climate change is of great concern for the society [Oki and Kanae, 2006; Pall et al., 2011; Min et al., 2011]. This is not only for providing a tangible basis to the design of early warning procedures and mitigation measures to avoid the loss of life and reduce damage but also for the assessment of their impacts on societies, which may be irreversible. In this context, the Mediterranean basin has a distinctive character that results from physiographic conditions. Köpen [1936] defines the Mediterranean climate as one in which winter rainfall is more than 3 times the summer rainfall, and Xoplaki et al. [2004] show that wet season precipitation from October to March, accounts for 50–60% (western and northern regions) and 70–90% (southern and eastern regions) of the annual total amounts (see their Figure 1d). Frei and Schär [1998] show that during the fall season local precipitation maxima are located near the Alpine foothills in southern France, in contrast with the typical Alpine rainy season which occurs during the main convective season from May to September, while a pronounced dry period is present in Mediterranean climates. The medium to high mountains that surround the Mediterranean Sea play a crucial role in steering air flow and the Mediterranean Sea acts as a moisture and heat reservoir, so that energetic mesoscale atmospheric features can evolve to heavy precipitation [e.g., Alpert et al., 2002; Tarolli et al., 2012; Reale and Lionello, 2013]. This is especially the case in the Northwestern Mediterranean. In autumn, high sea surface temperature can destabilize air masses and favor latent heat release which can produce heavy precipitations [Ducrocq et al., 2002, 2008; Lebeaupin et al., 2006]. Sea surface temperature variability can also modulate heavy precipitation at longer time scales (typically submonthly)

©2016. The Authors.

This is an open access article under the terms of the Creative Commons Attribution-NonCommercial-NoDerivs License, which permits use and distribution in any medium, provided the original work is properly cited, the use is non-commercial and no modifications or adaptations are made.

time scale) [Lebeaupin-Brossier *et al.*, 2013; Berthou *et al.*, 2014, 2015, 2016]. Conversely, Mediterranean summer is characterized by high temperatures, lack of rainfall, and long periods of drought [Stéfanon *et al.*, 2012, 2014]. The precipitation is mostly due to inland moisture advection by sea breeze [Bastin *et al.*, 2005, 2007], enhanced along the surrounding mountain slopes by anabatic winds [Bastin and Drobinski, 2005, 2006].

The response of precipitation extremes to warming is one of the key uncertainties associated with climate change. The Mediterranean area is already very sensitive to climate change at short (decadal) and long (millennial) time scales. In Spain, Quereda Sala *et al.* [2000] reported an increase of the mean annual temperature of  $0.5^{\circ}\text{C}$  to  $1.2^{\circ}\text{C}$  between 1870 and 1996. A similar trend is observed in France [Moisselin *et al.*, 2002]. When considering only the summer surface air temperature, the warming trend over the Mediterranean region for the period 1950–1999 was  $0.08^{\circ}\text{C}$  per decade [Xoplaki *et al.*, 2003], reaching the value of  $0.1^{\circ}\text{C}$  per decade for 1976–2000 [Solomon *et al.*, 2007], one of the highest rates over the entire globe. Precipitation intensity is projected to increase in most regions under warmer climates, and the increase in precipitation extremes will be larger than that in the mean precipitation [Meehl *et al.*, 2007]. In the Mediterranean region, the majority of the 21st century scenarios shows a decrease in average precipitation with a peak signal in summer with either atmosphere-ocean Global Climate Models (GCM) [Giorgi and Bi, 2005], atmosphere Regional Climate Models (RCM) [Gibelin and Déqué, 2003; Déqué *et al.*, 2005; Gao *et al.*, 2006; Ulbrich *et al.*, 2006], or coupled atmosphere-ocean Regional Climate Models (AORCM) [Somot *et al.*, 2007]. There is, however, no consensus on the evolution of the frequency and intensity of the extreme events over the Mediterranean regions, even though an increase in precipitation variability during the dry warm season is expected [Giorgi, 2006] and an increased probability of occurrence of events conducive to floods has been suggested [Gao *et al.*, 2006]. Globally, Giorgi [2006] defines the Mediterranean area as one of the two main “hot spots” of climate change, with an increase in the interannual variability in addition to a strong warming and drying.

To obtain a deeper insight on the evolution of the precipitation extremes intensity in a changing climate, the scaling of precipitation extremes with temperature is often used as a predictor [Allen and Ingram, 2002]. Indeed, the increase in the atmospheric water-holding capacity associated with a temperature increase (described by the Clausius-Clapeyron (CC) relation) considerably influences the changes in the extreme precipitation intensity under warmer climates [Betts and Harshvardhan, 1987; Trenberth *et al.*, 2003; Held and Soden, 2006]. Studies based on numerical models have revealed that the rate of increase in the extreme daily precipitation associated with atmospheric warming is consistent with that of the CC relation ( $\sim 7\% \text{ }^{\circ}\text{C}^{-1}$ ) [Allen and Ingram, 2002; Pall *et al.*, 2007; Kharin *et al.*, 2007]. High-resolution cloud-resolving simulations show a close agreement between the amplification of precipitation extremes with warming and the CC relation in the subcloud layer; in other words precipitation extremes increase following the humidity in the low troposphere [Muller *et al.*, 2011; Romps, 2011]. However, deviation from the CC scaling is feasible given the changes in the atmospheric dynamics [O’Gorman and Schneider, 2009a; Sugiyama *et al.*, 2010; Singleton and Toumi, 2013; Muller, 2013]. Hence, the applicability of the CC scaling is still undetermined. Recently, a study based on in situ data found that in De Bilt, the Netherlands, the extreme daily precipitation intensity increased along with the daily surface air temperature at a rate similar to the CC rate ( $7\% \text{ }^{\circ}\text{C}^{-1}$  globally) [Held and Soden, 2006; O’Gorman and Muller, 2010] in the daily surface air temperature range below  $8\text{--}10^{\circ}\text{C}$  and at a sub-CC rate at high temperatures [Lenderink and van Meijgaard, 2008]. A similar increase in the extreme precipitation intensity was found on the hourly time scale, except that the rate of increase in the intensity at high temperatures was larger than the CC rate (the so-called “super-CC rate”). A change in the relative contributions of large scale and convective precipitation was proposed as a possible cause for this super-CC rate [Haerter and Berg, 2009; Lenderink and van Meijgaard, 2009; Berg and Haerter, 2013; Berg *et al.*, 2013; Westra *et al.*, 2014; Molnar *et al.*, 2015]. Following the framework of the study conducted in De Bilt, a study based on a gridded  $0.44^{\circ}$ -resolution observational data set covering all of Europe revealed that the extreme daily precipitation intensity increases with daily surface air temperature in winter (this increase is limited by the CC relation) and that the intensity decreases with an increase in daily surface air temperature in summer [Berg *et al.*, 2009]. In Australia, the extreme daily precipitation intensity from in situ data was found to increase with daily surface air temperature up to  $20\text{--}26^{\circ}\text{C}$  and decrease at higher temperatures [Hardwick Jones *et al.*, 2010]. The rate of increase in the extreme daily precipitation intensity was not necessarily consistent with the CC rate. A CC-like rate was found only for time scales shorter than 30 min. Haerter *et al.* [2010] and Utsumi *et al.* [2011] investigated the effects of temporal resolution on the scaling of precipitation. The analysis by Utsumi *et al.* [2011] using subhourly time scale data in Japan revealed that the decrease in the extreme daily precipitation intensity at high temperatures was well explained by the decrease in the duration of the precipitation events, not by the decrease in

the precipitation intensity of individual storms. Extreme precipitation intensity at a 10 min time scale does not decrease even at high temperatures, where the extreme precipitation intensity at a daily time scale decreases. When the time scale is reduced from daily to 10 min, the rate of increase in the extreme precipitation intensity approaches the CC rate. Further studies are necessary to investigate whether the extreme precipitation on short time scales in other regions, especially in the regions where the CC scaling at daily time scale was not applicable, shows an increase similar to the CC rate. If so, the study by *Utsumi et al.* [2011] suggests that the temperature increase will increase the potential of severe extreme precipitation at a rate similar to the CC rate on short time scales, which would cause flash floods in cities and small catchments.

In the present study, we investigate the sensitivity of precipitation extremes to temperature in present-day climate variability, in the Mediterranean region. The applicability to climate change is not straightforward, but we believe that it sheds some light into the physical mechanisms which are important for extreme rainfall rates. The increase of atmospheric humidity with warming, at a rate close to the Clausius-Clapeyron thermodynamic rate, gives a first-order estimate for the change of precipitation extremes with temperature. But in the Mediterranean region, the dynamics can also play an important role, especially during strong "Cevenoles" events. We are particularly interested in departures from the Clausius-Clapeyron thermodynamic expectation, due in part to contributions from the dynamics. In this work, we rely on a dense observation network, fine scale gridded reanalysis and simulations performed in the context of HyMeX [Drobinski et al., 2014] and MED-CORDEX programs [Ruti et al., 2015]. Our goal is to investigate the temporal and spatial variability of this scaling. More precisely, we address the following questions:

1. How do precipitation extremes scale with temperature? Is it consistent with the thermodynamic CC scaling?
2. Is there a strong seasonal variability of the scaling, with large precipitation amounts during fall and winter, and arid situations during summer?
3. Can departures from the CC scaling be related to changes in the dynamics and/or changes in precipitation efficiency?

The next section details the data and model used for this study. Section 3 analyzes the precipitation extremes change with respect to temperature, its sensitivity to time and spatial averaging, and its spatial variability in the coastal mountainous region. Section 4 analyzes the various processes that affect the scaling of precipitation extremes with temperature and yield departures from CC scaling. Section 5 provides an in-depth discussion and elements of perspective with respect to regional climate change and concludes the study.

## 2. Material and Methods

### 2.1. Measurements

To investigate the precipitation extremes-temperature relationship, we selected stations spread over Southern France allowing the sampling of the mountainous area, the coastal band, and the inland plains of the investigated region (Figure 1b). Only stations with at least 30,000 accurate quality-checked 3-hourly temperature and precipitation data from 1989 to 2008 are included. The number of selected surface weather stations is 220 (see dots in Figure 1b).

Atmospheric integrated water vapor measurements from three Global Positioning System (GPS) stations have also been used to evaluate the ability of the simulations described in the following subsection to reproduce the water vapor content which partly controls precipitation (see red crosses in Figure 1b).

We also use the 2 m temperature and rain data provided every 3 h at 8 km horizontal resolution by the SAFRAN analysis system [*Le Moigne*, 2002] at the locations of the weather stations. The SAFRAN analysis system has been used to develop a long-term meteorological reanalysis over the French Alps [Durand et al., 1993, 2009] and then has been extended over the whole country and modified in order to feed macroscale soil-vegetation-atmosphere transfer models [*Le Moigne*, 2002]. Such data set is used because it is often a reference data set for local-scale precipitation and temperature climatologies as well as regional climate studies [e.g., *Lavaysse et al.*, 2012; *Vrac et al.*, 2012] even though some caution must be taken with gridded data sets in poorly sampled mountainous regions [*Flaounas et al.*, 2012]. It also provides a measurement-based data set without "holes" in the data collected by the surface weather stations. SAFRAN uses an optimal interpolation method to analyze most of the parameters. First, SAFRAN does a quality control of the observations. This is an iterative procedure based on the comparison between observed and analyzed quantities at the observation location. The analyses of temperature, humidity, wind speed, and cloudiness are performed every 6 h using all available observations. The first guess comes from the French large-scale operational weather

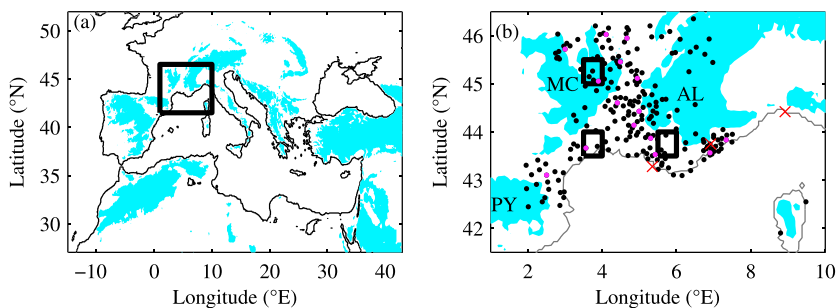


**Figure 1.** (a) Simulation domain of the HyMeX/MED-CORDEX regional climate simulations with the blue-shaded area indicating a topography higher than 500 m. The thick box indicates the region of interest for this study. (b) Zoom of the region of interest. The dots correspond to the locations of the surface weather stations operated by Météo-France used in this study. The magenta dots are a subset of stations used to investigate the effect of spatial averaging on the scaling of precipitation extremes with temperature (see text). The red crosses correspond to the locations of the GPS stations used to retrieve the atmospheric integrated water vapor. The three boxes correspond to three regions over which precipitation efficiency is computed in this study. The acronyms PY, MC, and AL stand for the Pyrénées, Massif Central, and the Alps mountains.

prediction model ARPEGE or from the European operational archives from ECMWF. The analysis is performed in two stages. In the first stage the vertical profiles of temperature, wind speed, humidity, and cloudiness are analyzed. These profiles are calculated with a vertical step of 300 m. In the second stage SAFRAN determines the surface parameters, using a cruder method. The first guess is, in this case, deduced and updated from the result of the previous analyses. The precipitation analysis is performed daily at 0600 UTC, to include in the analysis the numerous rain gauges that measure precipitation on a daily basis (in particular, in the climatological and snow networks). The first guess is in this case deduced from climatological fields (a constant altitudinal gradient or more elaborate fields, e.g., depending on weather type, if available). Next, the analyzed values are interpolated to an hourly time step. To this purpose, all altitude profiles (temperature, humidity, and cloudiness) and surface wind are linearly interpolated, solar (direct and diffuse) and longwave radiation are calculated using a radiative transfer scheme, which uses the vertical profiles previously calculated. The analysis of temperature at 2 m is slightly corrected at 1200 UTC using the daily observed maximum and is then adjusted hourly using the solar radiation and a relaxation to an equilibrium temperature. To keep the moisture content of the air constant, some corrections to the surface humidity are also applied. Finally, the determination of the hourly precipitation is solved in four steps: (1) determination of the highest hourly 0°C isotherm; (2) determination of the hourly snow-rain transition altitude, based on vertical temperature gradient; (3) determination of the daily rain-snow ratio based on the observed or estimated rain-snow ratio at each observation site; and (4) last, the hourly precipitation and phase are estimated, using the relative humidity and with the constraint of the daily rain-snow ratio. The hourly redistribution of precipitation is performed by weighting the total daily rainfall with humidity. The number of stations, used each day in SAFRAN, evolves with time [see Vidal *et al.*, 2010, Figure 2]. Continuously increasing from 3000 to 4000 observations per day for precipitation between the late 1950s to the present, the increase was much sharper for temperature, with a jump from 500 to 4000 stations per day between the late 1980s and the late 1990s (no significant change since then). A detailed description of SAFRAN, its validation and application over France is given by Quintana-Seguí *et al.* [2008]. In our study, we kept a homogenized temperature and rainfall data set over a 20 yr period between 1989 and 2008 (only nonzero observed precipitation).

Figure 2 shows the time series of the 3-hourly precipitation from the in situ weather station having the longest record and from the SAFRAN analysis at the nearest grid point. The daily precipitation data from SAFRAN analysis is also shown as the 3-hourly precipitation results from daily precipitation measurement processing. In general, the precipitation extremes from the weather station are more intense than those from the SAFRAN analysis. Figure 2 also zooms on one period to better illustrate the comparison between the data sets and shows a fairly good ability of the SAFRAN analysis to reproduce subdaily precipitation, i.e., the diurnal cycle of the precipitation.

Some of the weather surface stations, GPS data as well as the SAFRAN analysis have been uploaded to the HyMeX database in the frame of the long observation period (see Drobinski *et al.* [2014] for details on the observation strategy).

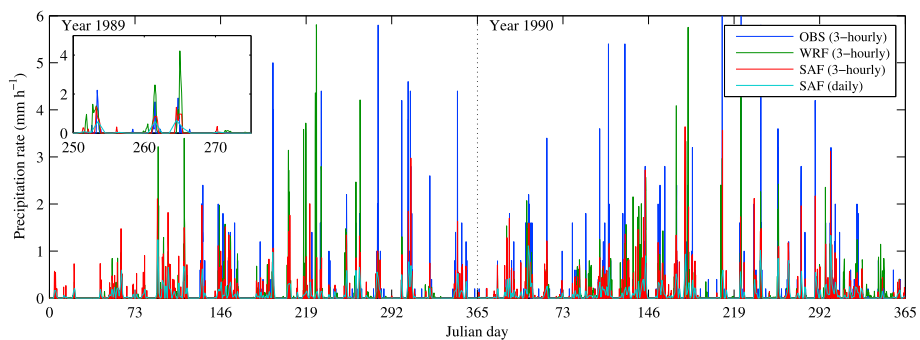


**Figure 2.** Time series of 3-hourly precipitation data from the in situ weather station having the longest record (blue), from the WRF simulation (green), and SAFRAN analysis (red) at the nearest grid point, as well as the daily precipitation data from SAFRAN analysis (cyan). The insert is a zoom over a time period allowing the comparison of the timing of the precipitation between the various data sets (between Julian day 250 and 275 of year 1989).

## 2.2. HyMeX/MED-CORDEX Simulations

The model used to downscale ERA I in the framework of MED-CORDEX [Ruti *et al.*, 2015] and HyMeX [Drobinski *et al.*, 2014] is the version 3.1.1 of the Weather Research and Forecasting Model (WRF). WRF is a limited area model, nonhydrostatic, with terrain following eta-coordinate mesoscale modeling system designed to serve both operational forecasting and atmospheric research needs [Skamarock *et al.*, 2008]. The WRF simulation has been performed with a 20 km horizontal resolution over the domain shown in Figure 1a between 1989 and 2011 with initial and boundary conditions provided by the ERA I reanalysis and updated every 6 h [Dee *et al.*, 2011]. Only the 1989–2008 time period was kept in the analysis for consistency with the period covered by the measurements (year 1989 is reliable for analysis as spin-up is very short due to the use of nudging). In the vertical, 28 unevenly spaced levels are used and the atmosphere top is at 50 hPa (sensitivity tests have been performed with more vertical levels without significant differences; 28 levels is the optimal choice for climate simulations with regard to both CPU time and data storage). The sea surface temperature is provided by ERA I. The geographical data are from 5 min resolution United States Geophysical Survey data. Soil type is based on a combination of the 10 min 17 category United Nations Food and Agriculture Organization soil data and U.S. State Soil Geographic 10 min soil data. The set of parameterizations used for these simulations include the WRF Single-Moment five-class microphysical parameterization [Hong *et al.*, 2004], the Kain-Fritsch convective parameterization 2004, the Dudhia shortwave radiation [Dudhia, 1989] and Rapid Radiative Transfer Model longwave radiation [Mlawer *et al.*, 1997], the Yonsei University planetary boundary layer scheme [Noh *et al.*, 2003], and the Rapid Update Cycle (RUC) land-surface models [Smirnova *et al.*, 1997]. The WRF simulation has been relaxed toward the ERA I large-scale fields (wind, temperature, and humidity) with a nudging time of 6 h [Salameh *et al.*, 2010; Omrani *et al.*, 2013, 2015]. Figure 2 compares the 3-hourly precipitation from the WRF simulation with the measurements from the weather surface station and the data from SAFRAN analysis. Despite differences in intensity which can be large, the event occurrences as well as the timing of the precipitation are fairly well reproduced. More in-depth comparison is given in the following.

The simulated precipitation and temperature have been evaluated against ECA and D gridded products at the Mediterranean basin scale [Flaounas *et al.*, 2013]. Other studies using this simulation [Lebeaupin-Brossier *et al.*, 2013; Stéfanon *et al.*, 2014; Chiriaco *et al.*, 2014] or ocean/atmosphere coupled simulations using WRF with such configuration [Drobinski *et al.*, 2012; Lebeaupin-Brossier *et al.*, 2013, 2015; Berthou *et al.*, 2014, 2015, 2016; Flaounas *et al.*, 2015] have already been published, and data can be found on the HyMeX/MED-CORDEX database.

## 2.3. Methods

In this study, the methodology proposed by Hardwick Jones *et al.* [2010] is followed. At each station for a given measurement duration (daily or 3-hourly), the maximum recorded precipitation rate on each rainy period is paired with the daily mean air temperature at 2 m above ground level. For the simulations, a threshold of 0.1 mm is applied to distinguish between rainy and nonrainy periods to reproduce a satisfactory rainfall distribution (indeed, in regional climate models with resolution typically larger than 10 km, very low intensity accumulated rainfall occurs too often). Three-hourly intensities are binned using the daily mean 2 m temperature instead of hourly temperatures, because we are interested in a proxy representing the temperature of

the air mass as well as for consistency with the previous works on the subject [e.g., *Hardwick Jones et al.*, 2010; *Haerter et al.*, 2010; *Westra et al.*, 2014]. For the temperature scaling from the SAFRAN analysis and regional climate simulations, we used the output of the grid points closest to the stations. The precipitation-temperature pairs are placed in 44 bins according to temperature, with an equal number of samples in each bin (50 samples) and therefore varying temperature ranges for each bin. A sensitivity analysis was conducted with increasing number of samples up to 200 without any significant difference. In each bin, 50 samples were finally used as the best trade-off between the temperature range sampling and the accuracy of the precipitation extreme estimate. The mean temperature of the events in each bin is used as the representative temperature for that bin. As in *Hardwick Jones et al.* [2010], this approach was preferred over using temperature bins of equal width, as it ensures a reasonable number of events across all bins. Within each bin of 50 samples, precipitation intensities are ranked to determine the 99th percentiles. An exponential regression is applied to the precipitation values for each percentile (by fitting a least squares linear regression to the logarithm of precipitation depth) to derive the slope of the temperature-precipitation extremes curve. When this slope is 0.065, it is equivalent to a Clausius-Clapeyron scaling of  $6.5\% \text{ }^{\circ}\text{C}^{-1}$  at  $15\text{ }^{\circ}\text{C}$ . Other methods have been applied in the literature, some including the dry days in the precipitation statistics [*O'Gorman*, 2012].

The analysis of the water budget in section 4 follows that of *Huang et al.* [2014]. It is conducted using the WRF simulations following the water budget formulation of *Braun* [2006] and *Yang et al.* [2011] to calculate the vapor, cloud, and precipitation budgets within the three boxes shown in Figure 1b and to compute the precipitation efficiency as defined in *Sui et al.* [2005, 2007]. The expression of precipitation efficiency  $\epsilon$  is

$$\epsilon = \frac{P}{\sum_{i=1}^4 Q_i^+} \quad (1)$$

The quantity  $P$  is the surface precipitation rate and  $Q_i = (Q_{\text{wvt}}, Q_{\text{wvv}}, Q_{\text{wve}}, Q_{\text{cm}})$  where  $Q_{\text{wvt}}$  is the local vapor change,  $Q_{\text{wvv}}$  is the water vapor convergence,  $Q_{\text{wve}}$  is the surface evaporation rate, and  $Q_{\text{cm}}$  is the sum of local hydrometeor change and hydrometeor convergence. The quantity  $Q_i^+ = Q_i$  when  $Q_i > 0$  and  $Q_i^+ = 0$  when  $Q_i \leq 0$  [*Sui et al.*, 2007]. Other alternative expressions exist which however produce similar results [*Sui et al.*, 2007].

### 3. Scaling of Precipitation Extremes With Temperature

Figure 3 shows the daily and 3-hourly precipitation extremes (99th percentile) as a function of the daily mean temperature at the surface weather stations and from the SAFRAN analysis and the WRF simulations at the nearest grid point. The black solid line indicates the median values, and the lower and upper dashed lines delimiting the shaded area are the 20th and 80th percentiles, respectively. Looking at the precipitation extreme-temperature curve, two regimes emerge which form a hook shape: one at low temperatures (cooler than  $18\text{ }^{\circ}\text{C}$  for the in situ measurements and cooler than  $15\text{ }^{\circ}\text{C}$  for WRF simulation and SAFRAN analysis) and one at high temperatures (warmer than  $18\text{ }^{\circ}\text{C}$  for the in situ measurements and warmer than  $15\text{ }^{\circ}\text{C}$  for WRF simulation and SAFRAN analysis). This behavior is surprisingly robust throughout the domain and for all percentiles. The slope at low temperatures is steeper and closer to the CC scaling than the slope at high temperatures. There is an impact of time averaging, with generally weaker slopes at daily time scales. However, whatever the time sampling, Figure 3 shows that the studied region does not seem to exhibit super CC behavior (except in the observations at individual locations, due in large part to the uncertainty of the fit; see later in the text), unlike what was found in other observational studies [e.g., *Lenderink and van Meijgaard*, 2008]. Instead, sub-CC scaling is found above a temperature of  $\sim 15\text{--}18\text{ }^{\circ}\text{C}$ , against a value of  $\sim 20\text{--}25\text{ }^{\circ}\text{C}$  in some previous works [e.g., *Utsumi et al.*, 2011]. *Berg et al.* [2013] point out that a change in slope can be due to the change in dominant precipitation type from large-scale to convective precipitation. In the WRF simulations, the decrease of slope at warm temperatures remains even when analyzing large-scale and convective precipitation separately (not shown).

In general, the slope is closer to CC scaling in observations than in the SAFRAN analysis and WRF simulations. Especially at high temperatures, a lower slope is found in the simulations. A possible explanation is given by *Singh and O'Gorman* [2012] who show that the scaling of the precipitation extremes with temperature is sensitive to the microphysics. Precipitation extremes are found to be sensitive to the fall speeds of hydrometeors, and this partly explains the different scaling results obtained with different microphysics schemes. A second explanation is the temperature range over which the slope is computed. Indeed, there is a warm bias

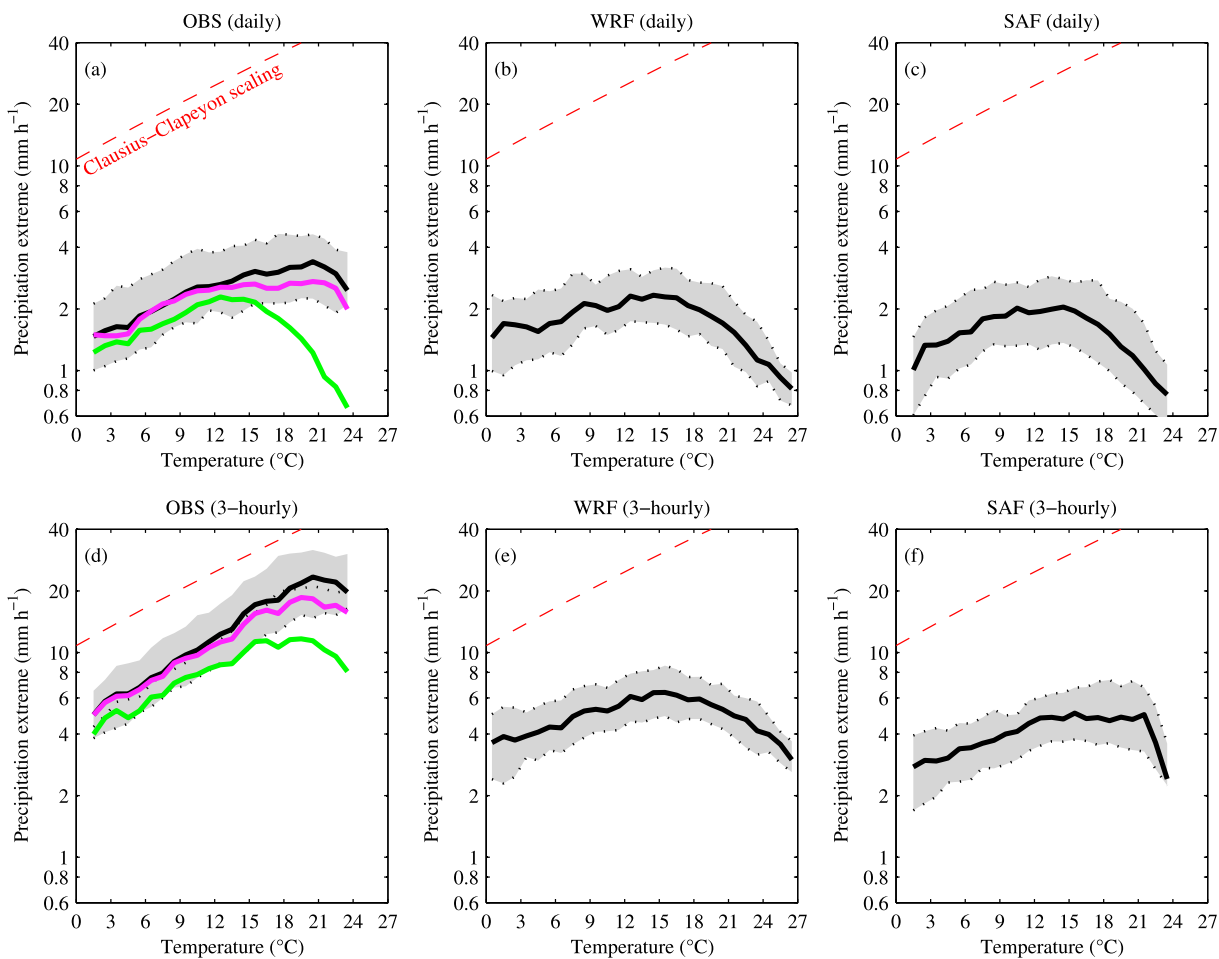


**Figure 3.** Precipitation extremes (99th percentile) versus daily averaged temperature from (a, d) surface weather stations (OBS) and from (b, e) WRF simulations (WRF) and (c, f) SAFRAN analysis (SAF) at the nearest grid point. The thick black line corresponds to the ensemble average at the surface weather station locations. The lower and upper dotted lines delimiting the shaded area are the 20th and 80th percentiles, respectively. The thick magenta and green curves display the curve retrieved from the in situ measurements corrected for the ratio of spatially averaged to local precipitation extremes over an area of about  $8 \times 8 \text{ km}^2$  and  $20 \times 20 \text{ km}^2$ , respectively (see Figure 4). These curves mimic the expected SAFRAN and WRF scaling, respectively. The dashed red line indicate the CC slope using the August-Roche-Magnus approximation for saturated vapor pressure.

in the WRF simulation of the maximum daily averaged temperature associated with precipitation extremes (+3.36°C compared to the surface weather station measurements). A third possible explanation is the impact of resolution [Eggert *et al.*, 2015]. Idealized simulations suggest that the amplitude of precipitation extremes is sensitive to resolution (with weaker values at coarser resolution where more averaging is applied), but its sensitivity to warming is not. Indeed, Romps [2011] and Muller *et al.* [2011] found a similar rate of increase of precipitation extremes with temperature in simulations at 200 m and 4 km horizontal resolution, respectively. Despite in-depth validation and critical assessment of the WRF simulations' performance in correctly reproducing the relevant processes associated with precipitation extremes in this region [e.g., Flaounas *et al.*, 2013; Lebeaupin-Brossier *et al.*, 2013; Berthou *et al.*, 2014, 2015, 2016], we can not rule out that in our more realistic setting, resolution could quantitatively impact our results. In order to investigate the spatial averaging issue, 15 stations surrounded by more than one station within an 8 and 20 km range have been selected. The range from each of the selected weather station typically corresponds to the SAFRAN and WRF resolutions. The 15 weather stations are shown in magenta in Figure 1b. The time series of precipitation of the weather stations present within the corresponding range (8 or 20 km) are averaged and reprocessed to derive the scaling of the precipitation extremes with daily precipitation. The ratio of the spatially averaged to local precipitation extremes as a function of daily temperature is shown in Figure 4. It shows that the effect of spatial averaging increases with the size of the averaging area. At cold temperature, the effect is small. This can be interpreted by the nature of the precipitation. They are caused by long lasting frontal bands which travel from west to

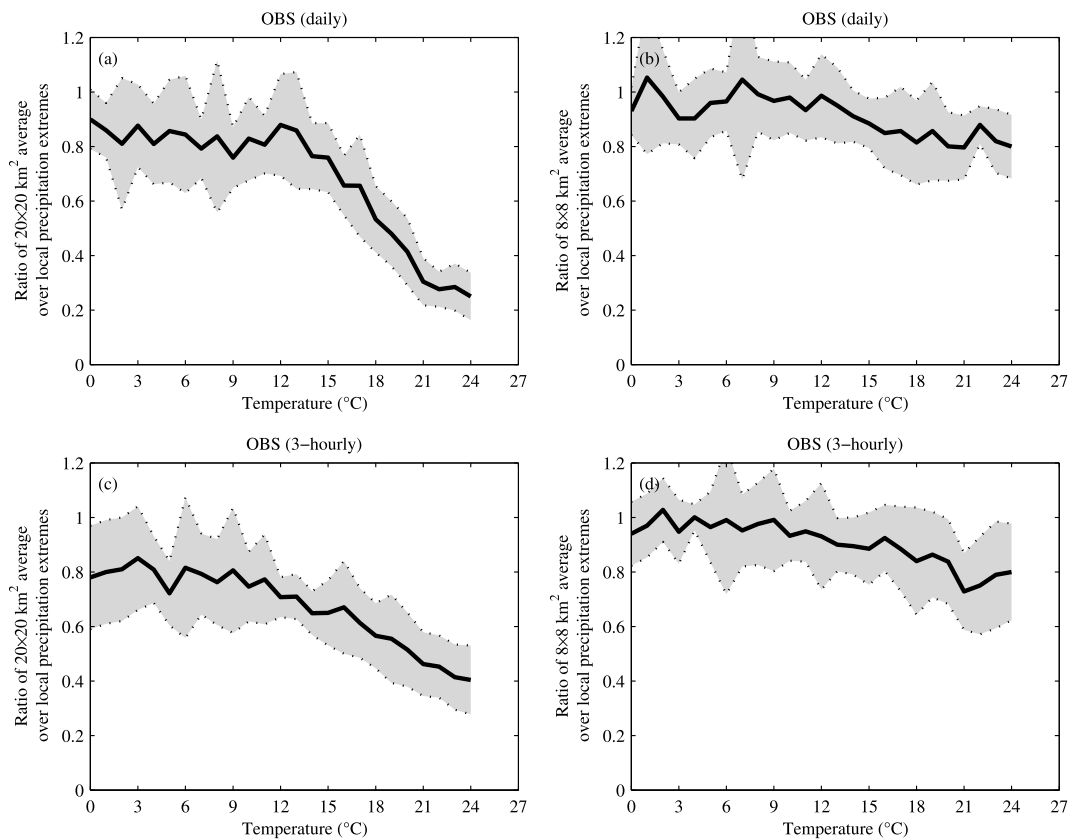


**Figure 4.** Ratio of daily and 3-hourly precipitation extremes as a function of daily temperature recorded by 15 weather stations shown in Figure 1b (magenta dots) spatially averaged over a 20 km and 8 km range with the surrounding available weather stations to that of the local weather station. The thick black line corresponds to the ensemble average at the 15 surface weather stations locations (Figure 1b). The lower and upper dotted lines delimiting the shaded area are the 20th and 80th percentiles, respectively.

east. They cover a large area and last for several hours. In that situation, the effect of both space and time averaging is not significant. Conversely, at warm temperatures, the averaging effect has much more impact. The precipitations averaged over about a 20 × 20 km<sup>2</sup> area are much weaker than those measured at one single weather station. This effect is similar when considering 3-hourly accumulated precipitation. When averaging over about an 8 × 8 km<sup>2</sup> area, the effect of spatial averaging is weaker.

The consequence of spatial averaging effect is consistent with *Chen and Knutson [2008]* and *Khodayar et al. [2016]* and is illustrated in Figures 3a and 3d which displays the curve drawn from the in situ measurements corrected using the ensemble mean ratio of spatially averaged to local precipitation extremes of Figure 4. The magenta and green curves mimic the expected SAFRAN and WRF scaling, respectively. The agreement between the simulated scaling of precipitation extremes and the “corrected daily precipitation” curve is improved. The hook shape is enhanced by spatial averaging. The temperature break, which is the temperature at which a sharp change in slope is observed, is also consistent between the simulation and the corrected daily precipitation curve. The impact of spatial averaging on the scaling of 3-hourly precipitation extreme is weaker but improves the comparison with the scaling from WRF simulation. Indeed, the scaling with and without correction are closer when considering 3-hourly precipitation extremes than when using daily precipitation extremes. The winter precipitation extremes are most accurately reproduced by both SAFRAN and WRF, whereas the most underestimated precipitation extremes are the summer precipitation extremes. Regarding SAFRAN, the weighting of daily precipitation by humidity to generate hourly precipitation is probably less reliable in a summer arid environment. The “plateau” between 15 and 20°C is more consistent with the corrected curve, but the steepening of the negative slope is too weak in the corrected daily precipitation curve. This can be attributed to the low number of stations within an 8 km range from each of the 15 stations. Regarding the WRF simulation, the simulated summer precipitations are largely dominated by parameterized precipitation

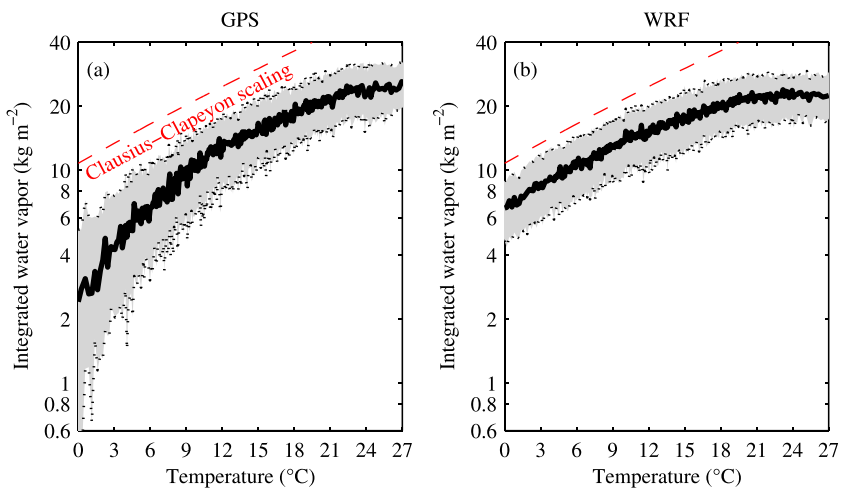


**Figure 5.** Atmospheric integrated water vapor versus daily averaged temperature from (a) GPS stations (GPS) and from (b) WRF simulations (WRF) at the nearest grid point. The thick black line corresponds to the ensemble average at the GPS station locations. The lower and upper dotted lines delimiting the shaded area are the 20th and 80th percentiles, respectively. The red dashed line indicates the CC slope using the August-Roche-Magnus approximation for saturated vapor pressure.

with respect to explicit precipitation and are thus very sensitive to the convection scheme [e.g., Cretat et al., 2012; Di Luca et al., 2014] which analysis is beyond the scope of this study. Despite these issues, accounting for spatial averaging effect gives therefore more confidence on the quality of the WRF simulations. As a complementary evaluation of WRF simulations, Figure 5 shows how WRF simulates the water vapor in the atmosphere which is a key variable controlling the scaling of heavy precipitation with temperature [e.g., Bretherton et al., 2004]. It displays a comparison between the integrated water vapor retrieved from the GPS data collected at the three GPS stations shown in Figure 1b and the integrated water vapor computed from the WRF simulations at the nearest grid point. Since the integrated water vapor is already a spatially averaged quantity, significant sensitivity of spatial averaging on integrated water vapor is here not expected. Figure 5 shows that WRF overestimates the integrated water vapor at temperatures colder than 6°C. Above, the simulations still display a weak positive bias but the shape of the curve is in excellent agreement with the GPS measurements. In particular, Figure 5 shows that above 20°C, the integrated water vapor saturates. Such behavior, which is not seen at higher latitudes is well captured by WRF and suggests a limitation of water vapor sources at such temperatures.

Regarding shorter 3-hourly time average, its main effect is a smaller reduction of the slope from cold to warm temperatures, with however a hook shape still visible at high temperatures. This is consistent with the results of Haerter et al. [2010] and Utsumi et al. [2011] who found that event duration decreases with temperature, which partly explains the difference between daily and 3-hourly slopes. Figure 6 shows the ratio of 3-hourly to daily precipitation extremes as a function of the daily temperature at the surface weather stations and from SAFRAN analysis and WRF simulations at the nearest grid point. The ratio equals 1 when the daily averaged precipitation reduced over a period of 3 h (i.e., divided by 8) is equal to the 3-hourly accumulated precipitation. It means that it rains all day, i.e., 8 times the 3-hourly precipitation. Conversely, when the ratio equals 8, it means that it only rains during 3 h this day so the daily average precipitation reduced over a period of 3-h is equal to one eighth of the 3-hourly maximum precipitation. The fact that the decrease in slope is larger for daily precipitation extremes than for 3-hourly precipitation extremes is due to warmer events having shorter durations. For those warm short events, taking a daily average adds zeros to the 3-hourly rainfall rate. This effect is present in the observations and in WRF simulation and SAFRAN analysis, though it is weaker for the latter two. Limitation of data (only 3-hourly or daily values) does not allow to address the issue of intermittency. Higher-frequency outputs than 3-hourly, which unfortunately were not available for these data sets, could yield slopes closer to CC.

Figure 7 shows the spatial pattern of the precipitation scaling with respect to the daily mean temperature computed over the temperature range below and above a temperature break. The temperature break is the temperature at which the slope of the temperature-precipitation extreme relation sharply changes. It differs

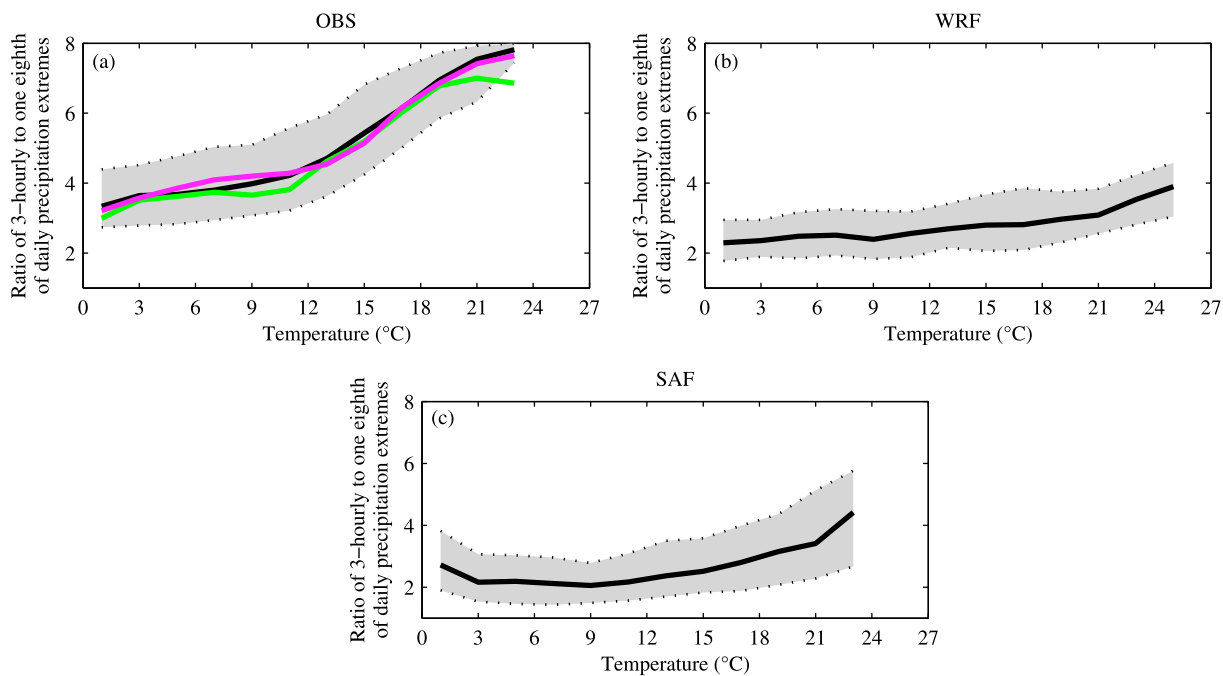


**Figure 6.** Ratio of 3-hourly to one eighth of daily precipitation extremes as a function of 2 m daily temperature at (a) the surface weather stations and interpolated at the stations location from (b) WRF simulations and (c) SAFRAN analysis. The daily average precipitation are reduced over a period of 3 h (i.e., divided by 8). The thick black line shows the mean value and the grey-shaded area the spatial variability around the mean. The thick magenta and green curves display the curve retrieved from the in situ measurements corrected for the ratio of spatially averaged to local precipitation extremes over an area of about  $8 \times 8 \text{ km}^2$  and  $20 \times 20 \text{ km}^2$ , respectively (see Figure 4). These curves mimic the expected SAFRAN and WRF scaling, respectively.

between the data sets. It is  $18^\circ\text{C}$  for the in situ measurements and  $15^\circ\text{C}$  for the WRF simulation and SAFRAN analysis. A quality control on the slope estimate is applied along the following procedure. A two-segment linear regression is fitted on the temperature–precipitation extremes relationship by using a least squares fitting. All possible breakpoints are tested (i.e., by using each temperature bin as breakpoint). The retained breakpoint corresponds to the two-segment linear regression that has the least squares. The slopes obtained for these two linear regressions are plotted in Figure 7. In order to limit border effects, if the breakpoint is obtained on the borders (five first and last temperature bins), a unique regression line is fitted. Thus, in this case, there is no temperature breakpoint. This occurs only for the weather surface measurements and SAFRAN analysis on the warm temperature side. This explains why dots are removed in the slope pattern for high temperatures. The agreement is good between the data sets. The slope retrieved from the WRF simulation for cold temperatures underestimates the slope computed from the data collected at the weather stations. The slope obtained from SAFRAN analysis ranges in between the two other data sets. For cold temperature, the slope is negative nearly everywhere. A comparison with a similar pattern for 3-hourly precipitation (Figure 8) shows that the averaging effect has less impact at cold temperature than at warm because of the time-averaging effect. The slope is less steep for warm temperature and 3-hourly precipitation than for daily precipitation. The in situ measurements also display a steeper positive slope at cold temperature with a super-CC over the mountains. It is also steeper in the WRF simulation and SAFRAN analysis but the change is weaker and the slope remains close to CC scaling. The patterns for both daily and 3-hourly precipitation display a weaker slope in the southwestern part of domain along the Pyrénées mountain range and along the coast. The origin of such behavior is not straightforward and is left for future work.

#### 4. Process Analysis

Establishing a relationship between precipitation and surface temperature (generally measured at 2 m), and comparison with the Clausius–Clapeyron equation appears not to be straightforward. No global picture emerges for the scaling of precipitation extremes with temperature, regional specificities apparently being a strong driver. Several factors can lead to disparities from the thermodynamic Clausius–Clapeyron

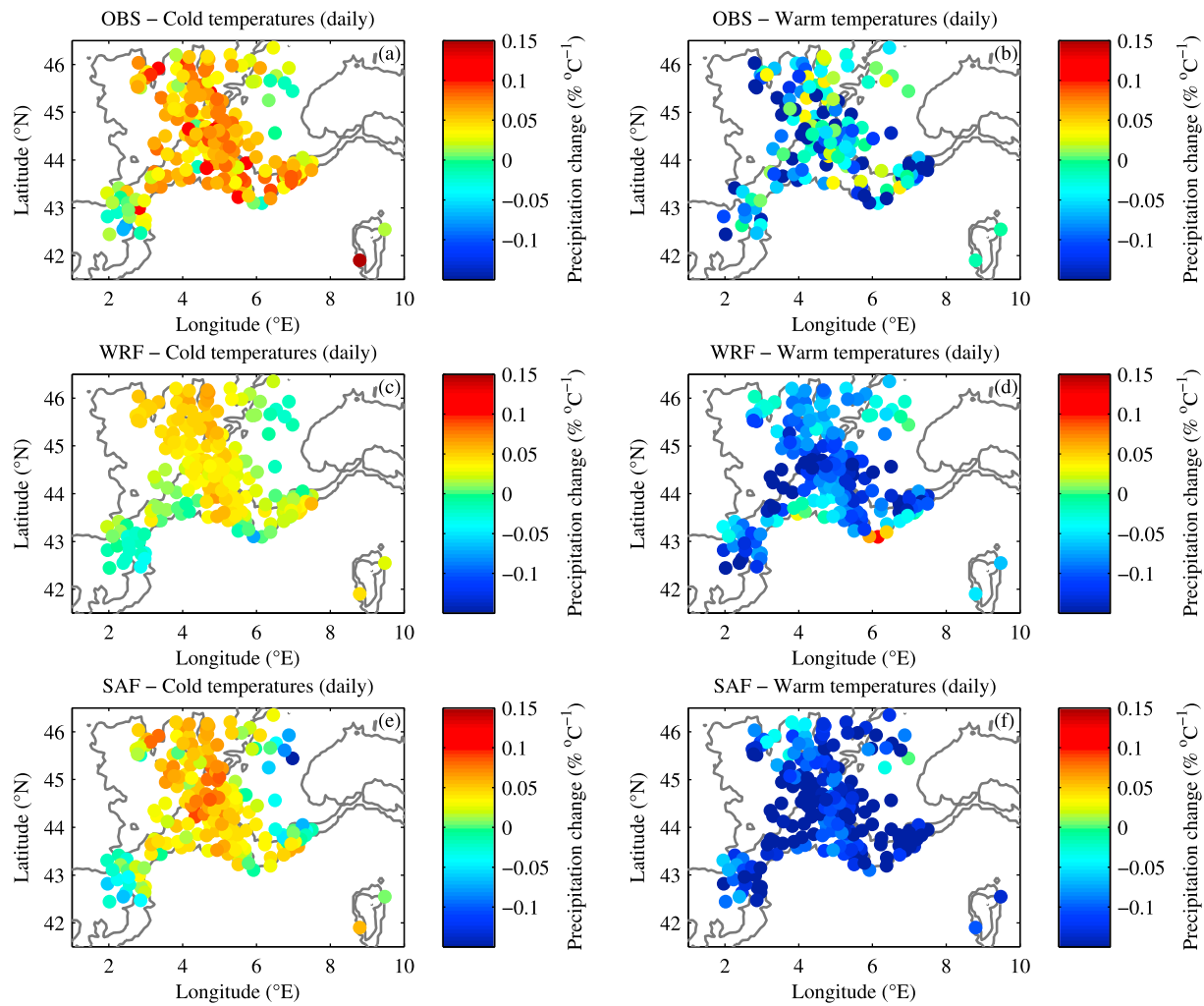


**Figure 7.** Precipitation change with respect to 2 m temperature ( $^{\circ}\text{C}^{-1}$ ) for daily precipitation from (a, b) surface weather stations, (c, d) WRF simulations, and (e, f) interpolated SAFRAN analysis for cold (Figures 7a, 7c, and 7e) and warm (Figures 7b, 7d, and 7f) temperatures. The iso-contours display the coastline and the 500 m altitude (see Figure 1). The threshold discriminating cold and warm 2 m temperatures is the temperature break identified in Figure 3 which marks the sharp variation of the slope. It is  $18^{\circ}\text{C}$  for the weather surface observations, and  $15^{\circ}\text{C}$  for WRF simulations and SAFRAN analysis. The CC scaling is about  $0.07\% \text{ }^{\circ}\text{C}^{-1}$ .

expectation. The Clausius-Clapeyron equation relates the saturation water vapor mixing ratio to the temperature of condensation. One can write that

$$P \propto \epsilon w Q_{\text{sat}} \quad (2)$$

where  $P$  is the precipitation rate,  $\epsilon$  the precipitation efficiency,  $Q_{\text{sat}}$  the saturation water vapor mixing ratio in the low troposphere where rising parcels start to condense, and  $w$  the maximum vertical velocity in the troposphere, which is reached in the vicinity of the clouds at high temperatures. The midtropospheric vertical velocity is also commonly used in precipitation extreme scalings [Betts and Harshvardhan, 1987; O'Gorman and Schneider, 2009b; Muller, 2013]. A sensitivity study has been performed on the scaling of precipitation extremes to the choice of the vertical velocity, without significant difference (not shown). The quantity  $Q_{\text{sat}}$  represents the maximum liquid water content formed in the condensation process. Differentiating with respect to a temperature  $T$  gives,

$$\frac{1}{P} \frac{\partial P}{\partial T} = \frac{1}{\epsilon} \frac{\partial \epsilon}{\partial T} + \frac{1}{w} \frac{\partial w}{\partial T} + \frac{1}{Q_{\text{sat}}} \frac{\partial Q_{\text{sat}}}{\partial T}. \quad (3)$$

Changes in precipitation efficiency and vertical transport with temperature  $T$  could partly explain departures from CC scaling. Another possible source of discrepancy is the choice of the temperature, which can lead to difference whether, for instance, condensation temperature  $T$  or near-surface temperature ( $T$  at 2 m) is used.

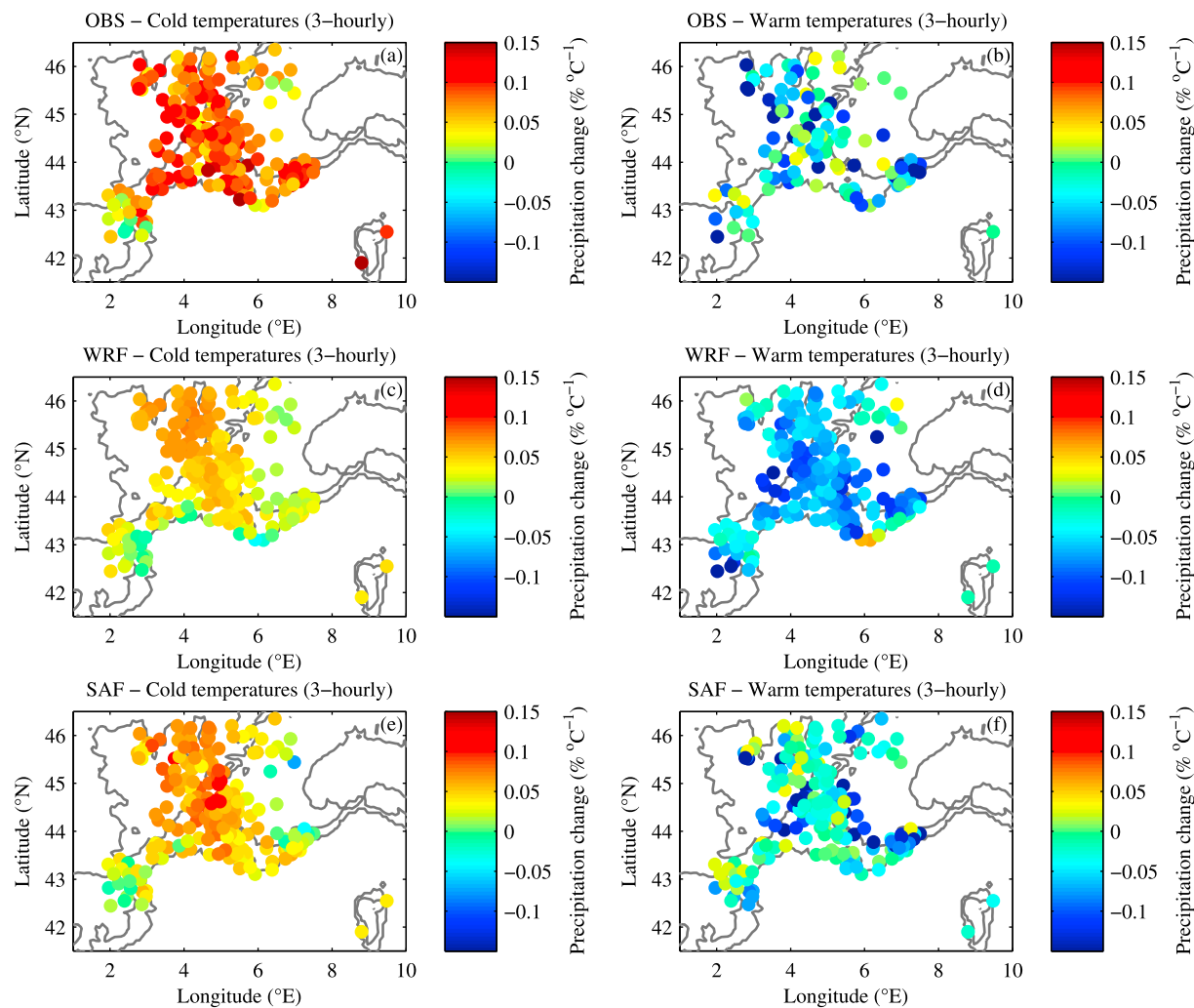


**Figure 8.** Same as Figure 7 but for 3-hourly precipitation.

The following analysis relies on the WRF simulation only as it provides all the needed diagnostic variables not only near the surface but also over the whole atmospheric column.

It is important to make clear that, in this study, the change of precipitation extremes with daily temperature for the present climate state is analyzed, in order to derive an “observed” scaling. How such scaling is linked to the “projected” scaling relating change of precipitation extremes with change of temperature over time or across climate states [e.g., Allen and Ingram, 2002] is not straightforward. However, better understanding the observed scaling is a necessary step to avoid misinterpretation of the projected scaling.

#### 4.1. Condensation Process

Let  $Q(T)$  be the water vapor mixing ratio in the atmospheric boundary layer at temperature  $T$ . The water vapor mixing ratio  $Q(T) = Q_{\text{sat}}(T_d)$ , where  $T_d$  is dew point temperature. There are two different ways for an air parcel characterized by a temperature  $T$  and a water vapor mixing ratio  $Q(T)$  to reach saturation.

1. It can reach the saturation by an increase of humidity in the atmospheric boundary layer. The saturation occurs at temperature  $T$  after the humidity in the boundary layer increases from  $Q(T)$  to  $Q_{\text{sat}}(T)$ .
2. In case it cannot reach the saturation by an increase of humidity because of, e.g., water vapor source limitation, the only possible way to reach saturation is to lift the air parcel so that it cools and reaches the dew point temperature. In this case, the maximum water vapor content that can condense is  $Q_{\text{sat}}(T_d) < Q_{\text{sat}}(T)$ .

Let us investigate the various possibilities of the change of saturation water vapor mixing ratio when the temperature increases from a temperature  $T_1$  to  $T_2$ :

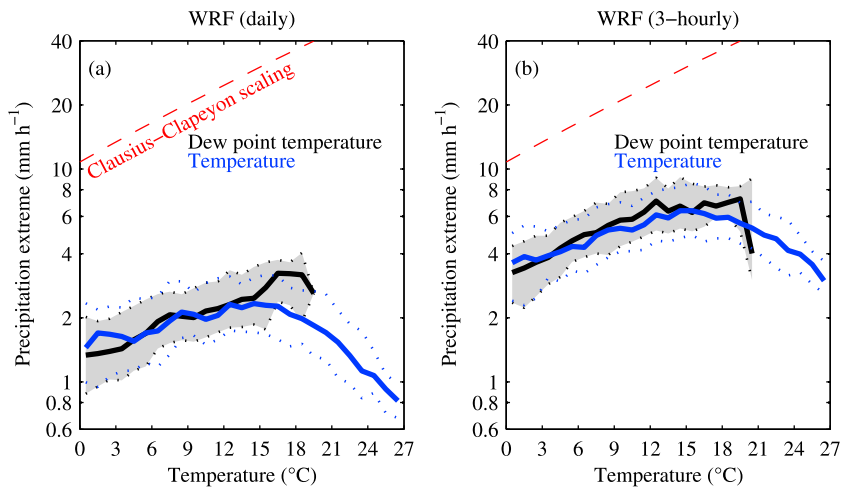


**Figure 9.** (a) Daily and (b) 3-hourly precipitation extremes (99th percentile) versus daily averaged dew point temperature (black curves) and air temperature (blue curves) from the WRF simulations at the nearest grid point of the surface weather stations (Figure 1). The thick lines correspond to the ensemble average at the surface weather locations. The lower and upper dotted lines delimiting the shaded area are the 20th and 80th percentiles, respectively. The red dashed line indicates the CC slope using the August-Roche-Magnus approximation for saturated vapor pressure.

1. Let us consider the air parcel close to saturation at  $T_1$  and  $T_2$  (high relative humidity, i.e.,  $T_{d,1} \sim T_1$  and  $T_{d,2} \sim T_2$ , as a first order of approximation). The maximum water vapor content that condenses is  $Q_{\text{sat}}(T_1)$  and  $Q_{\text{sat}}(T_2)$ . The change in saturation water vapor mixing ratio between  $T_1$  and  $T_2$  is thus  $Q_{\text{sat}}(T_2) - Q_{\text{sat}}(T_1)$  which follows a CC scaling.
2. Let us consider the air parcel close to saturation at  $T_1$  (high relative humidity, i.e.,  $T_{d,1} \sim T_1$ ) and far from saturation at  $T_2$  (low relative humidity, i.e.,  $T_{d,2} \ll T_2$ ). The maximum water vapor content that condenses is  $Q_{\text{sat}}(T_1)$  and  $Q_{\text{sat}}(T_{d,2}) < Q_{\text{sat}}(T_2)$ . The change in saturation water vapor mixing ratio between  $T_1$  and  $T_2$  is  $Q_{\text{sat}}(T_{d,2}) - Q_{\text{sat}}(T_1) < Q_{\text{sat}}(T_2) - Q_{\text{sat}}(T_1)$  which thus follows a sub-CC scaling.
3. Let us consider the air parcel far from saturation at  $T_1$  (low relative humidity, i.e.,  $T_{d,1} \ll T_1$ ) and close to saturation at  $T_2$  (high relative humidity, i.e.,  $T_{d,2} \sim T_2$ ). The change in saturation water vapor mixing ratio between  $T_1$  and  $T_2$  is  $Q_{\text{sat}}(T_2) - Q_{\text{sat}}(T_{d,1}) > Q_{\text{sat}}(T_2) - Q_{\text{sat}}(T_1)$  which thus follows a super-CC scaling.
4. Finally, let us consider the air parcel far from saturation at  $T_1$  and  $T_2$  (low relative humidity, i.e.,  $T_{d,1} \ll T_1$  and  $T_{d,2} \ll T_2$ ). The change in saturation water vapor mixing ratio between  $T_1$  and  $T_2$  is  $Q_{\text{sat}}(T_{d,2}) - Q_{\text{sat}}(T_{d,1})$ . If  $Q(T_1) < Q(T_2)$  then the slope of the change in saturation water vapor mixing ratio is positive and can be sub-CC, CC, and super-CC, as there is no straightforward relationship between the temperature in the boundary layer and the temperature at condensation. If  $Q(T_1) = Q(T_2)$  then there is no change and the slope is zero. If  $Q(T_1) > Q(T_2)$ , then the slope is negative and the scaling sub-CC.

If only condensation processes were involved in precipitation content (i.e., neglecting the impact of vertical transport and precipitation efficiency in equation (3)), one would expect precipitation change with respect to dew point temperature to follow a CC scaling [e.g., Lenderink *et al.*, 2011; Panthou *et al.*, 2014]. Figure 9 shows the daily and 3-hourly precipitation extremes (99th percentile) as a function of the daily mean dew point temperature and air temperature from the WRF simulations at the nearest grid point of the surface weather stations. As expected, the slope is slightly closer to the CC scaling but still exhibits variability, and overall the precipitation change rate with respect to dew point temperature remains sub-CC. Figure 10a displays  $Q_{\text{sat}}$  as a function of daily mean temperature, where  $Q_{\text{sat}}$  denotes the saturation mixing ratio at cloud base. It clearly exhibits a nearly perfect CC scaling up to 17°C. For temperature warmer than 17°C, the slope is sub-CC, probably due to a shift toward “low relative humidity” conditions and explains the impact, even though small, of using the dew point or the air temperature to compute the surface precipitation change at warm temperature. This behavior can easily be explained by the moisture limitation regime. At the highest temperature, corresponding to summer, the Mediterranean climate is arid. There is thus low moisture content available for precipitation. To condensate small moisture amount, the air parcel must be lifted up to high altitude to reach the condensation level. At this altitude, the temperature is much lower than the 2 m temperature causing a sub-CC scaling as explained above. The hook shape at high temperatures can thus be partly explained by the

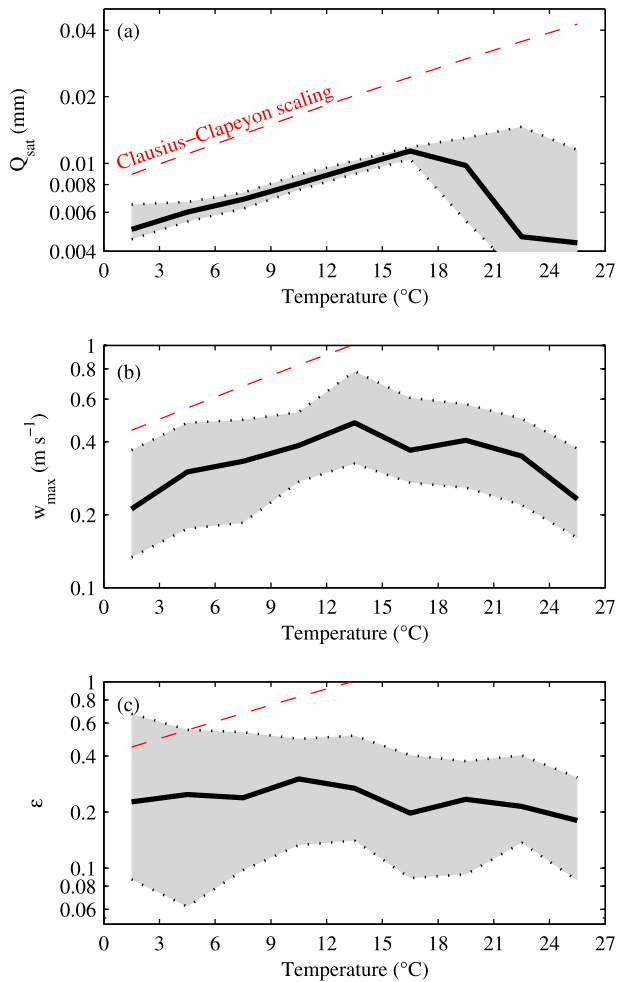


**Figure 10.** (a) Saturation water vapor content, (b) maximum vertical velocity, and (c) precipitation efficiency  $\epsilon$  computed from the WRF simulations for all extreme precipitation events over the whole atmospheric column of the three regions shown in Figure 1. The red dashed line indicates the CC slope using the August-Roche-Magnus approximation for saturated vapor pressure.

temperature break at  $15^{\circ}\text{C}$ , we randomly split the data set for one given temperature range into two and four subsets. For each subset we recompute the mean and standard deviation of all deciles ranging between the first (10th percentile) and eighth (80th percentile). The peak visible around the temperature break becomes significant for percentiles higher than the 70th percentile at 95% confidence level (not shown). The “peak” of the 50th percentile is therefore not significant, but it is significant above the 70th percentile. As will be discussed in detail in Figure 11, such difference can be seen as a seasonal hysteresis in the scaling of precipitation extremes with temperature. As explained in section 1, the French Mediterranean region has a specific precipitation extremes seasonality with fall season local precipitation maximum [Frei and Schär, 1998]. The lower vertical velocity percentile in Figure 10b corresponds to springtime precipitation extremes whereas the higher percentile to the fall time events, also called the “Cévenoles” events [e.g., Delrieu *et al.*, 2005].

Evidence of this is shown in Figure 11 which displays the occurrence of extreme precipitation as a function of temperature and precipitation intensity in winter (January–March), spring (April–June), summer (July–September) and fall (October–December). The occurrence is computed over temperature/precipitation bins of size  $3^{\circ}\text{C} \times 3 \text{ mm}$ . Figure 11 shows that between  $12$  and  $15^{\circ}\text{C}$ , three seasons contribute to rainfall but with two distinct modes identified as “mode 1” and “mode 2.” These two modes are visible during fall, while only one mode is visible during winter, summer, and spring. The peak of precipitation extremes (80th percentile), identified as “mode 2” in Figure 11d, is a mixture of precipitation extremes occurring in summer

use of the 2 m temperature as a proxy of the condensation temperature, in particular, over plains. However, there is a large spread of the slope at warm temperatures. As using the dew point temperature is not enough to obtain a CC scaling, the departure of precipitation change from CC scaling should also be attributed to processes other than condensation (precipitation efficiency, moisture transport) as will be discussed in the following section. Impact of grid resolution and intermittency are not addressed further in this work.

#### 4.2. Vertical Transport

Figure 10b displays the maximum vertical velocity over the whole atmospheric column, conditioned on precipitation. On average, the vertical velocity increases with temperature for all percentiles until about  $12^{\circ}\text{C}$ , whereas after  $15^{\circ}\text{C}$ , the trend is negative with vertical velocity decreasing with increasing temperature for all percentiles. When conditioned on dry days only, there is no significant trend (not shown). Figure 10b shows that between  $12$  and  $15^{\circ}\text{C}$ , which corresponds to averaged temperatures of spring and fall over this region, the percentiles differ significantly. The lower quantile shows a smooth transition and is relatively flatter than the 80th percentiles. Conversely the 80th percentile displays a pronounced peak. As the shape of the percentiles is of importance, there is a need to assess its significance. To analyze the significance of the peak of vertical velocity around the

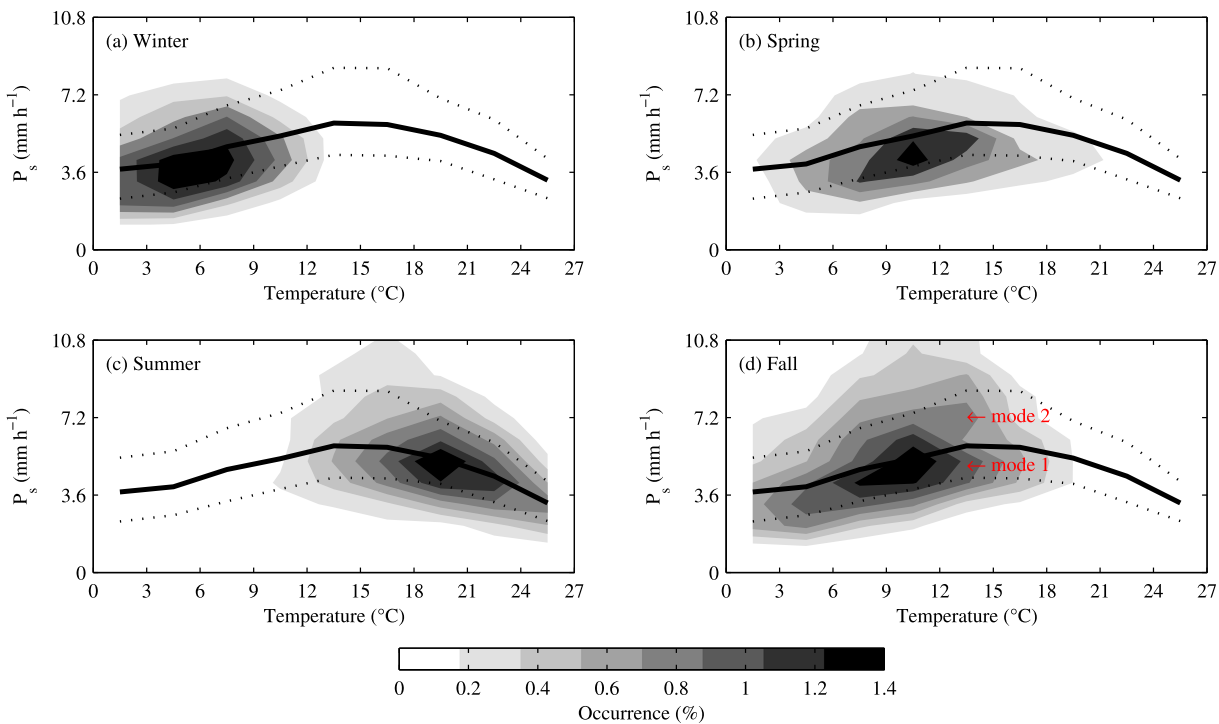
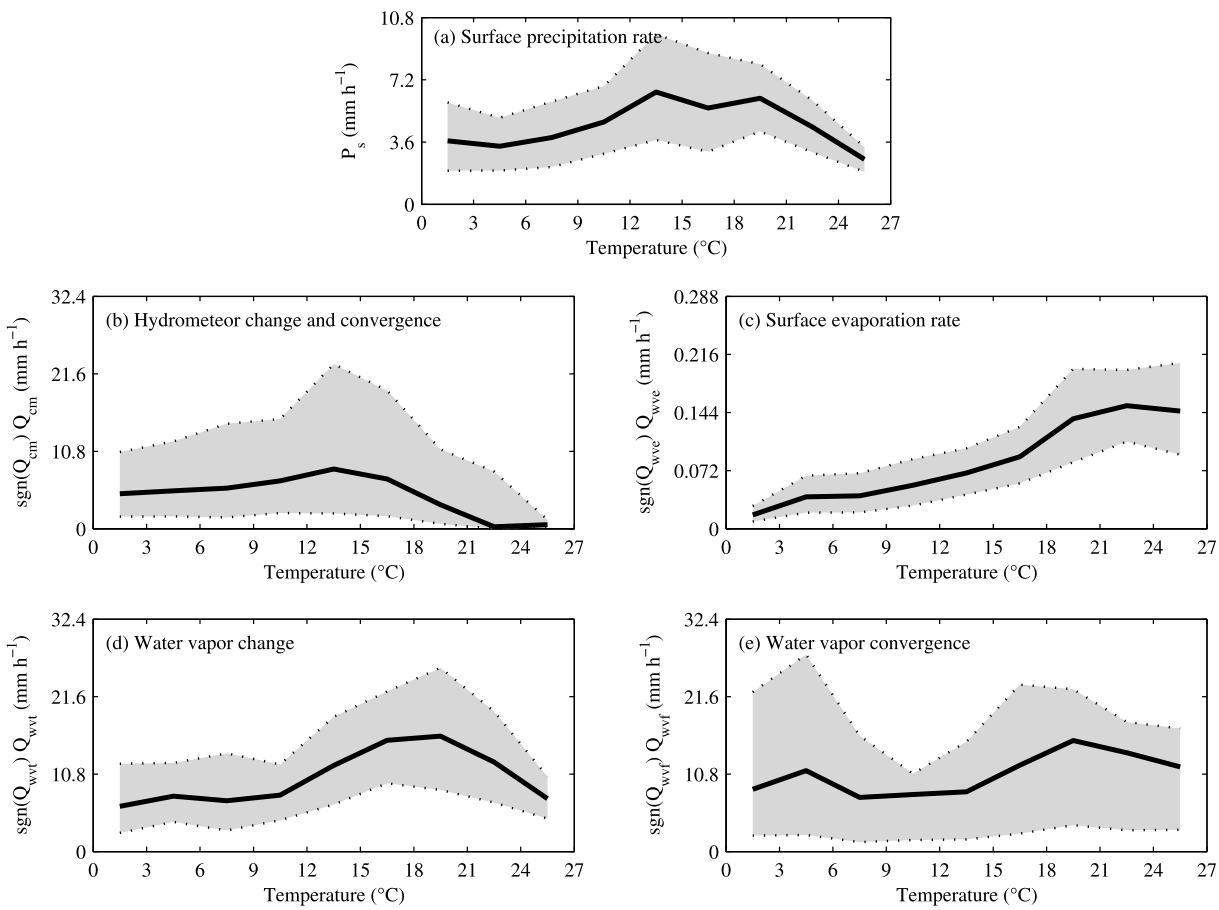


**Figure 11.** Occurrence of extreme precipitation computed from the WRF simulations as a function of daily temperature and 3-hourly precipitation intensity in (a) winter (January–March), (b) spring (April–June), (c) summer (July–September), and (d) fall (October–December). The thick lines and dotted lines correspond to the ensemble average and the 20th and 80th percentiles of precipitation extremes (see Figure 3).

and fall. The summer contribution to the peak is due to the month of September, included here in the summer season, which corresponds to the beginning of the “Cévenoles” episodes season [e.g., Delrieu *et al.*, 2005]. Such events, occurring typically between September and November, are characterized by a strong marine low-level jet which converges over the investigated area due to the blocking by the Alps and eventually impinges on the Massif Central where it is lifted and produces precipitation extremes [e.g., Bresson *et al.*, 2012]. The direct uplift of the strong low-level jet by the orography produces large vertical velocities which are evidenced in Figure 10b. The curve of the 20th percentile between 12 and 15°C, identified as “mode 1” in Figure 11d, is comparatively more flat. The precipitation extremes occurrence is similar to that around the 80th percentile and is associated with spring to fall episodes. The weakest precipitation events correspond to orographic precipitation triggered by convective instability along the mountain slopes, so the orography does not play a significant role in enhancing the vertical velocity. For temperature lower than 12°C, corresponding to winter and fall events, the precipitation extremes distribution is skewed toward lower values and correspond to frontal precipitation. For temperatures higher than 15°C corresponding to spring and summer events, the precipitation extremes distribution is also skewed toward lower values and correspond to convective precipitation. In both cases, orography plays a minor role in precipitation extremes triggering and so in vertical moisture transport enhancement. The fact that the vertical velocity decreases with temperature is due to the decrease of convective available potential energy caused by dilution with dry unsaturated environment air during summer. Indeed, rising saturated air parcels tend to be diluted by entraining some of the relatively dry unsaturated environment air. The entrainment of dry air and the evaporative cooling caused by entrainment reduces the buoyancy of the convective parcel. Mass entrainment also exerts drag on the entraining air parcel which thus undergoes less acceleration [Zhang, 2009; Holton and Hakim, 2013].

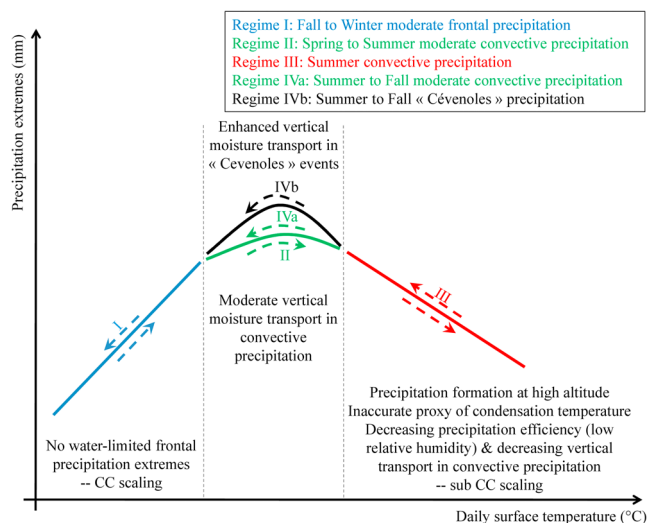
#### 4.3. Precipitation Efficiency

Figure 10c displays the precipitation efficiency  $\epsilon$  computed from the WRF simulations using equation (1) for all extreme precipitation events over the whole atmospheric column of the three regions shown in Figure 1. The various terms of the precipitation efficiency budget of equation (1) are displayed in Figure 12. In the two figures, the black solid line indicates the median values and the lower and upper dashed lines delimiting the



**Figure 12.** Terms of the precipitation efficiency budget of equation (1) computed from the WRF simulations for all extreme precipitation events over the three regions shown in Figure 1. (a) The quantity  $P$  is the surface precipitation rate, (b)  $Q_{cm}$  the sum of local hydrometeor change and hydrometeor convergence, (c)  $Q_{wve}$  the surface evaporation rate, (d)  $Q_{wvt}$  the local vapor change, and (e)  $Q_{wvf}$  the water vapor convergence. Note the different ranges of y values in the different panels.

shaded area are the 20th and 80th percentiles, respectively. Figure 12c shows that the surface evaporation rate increases with surface temperature until about 20°C where it "saturates" and remains quasi-constant as temperature increases due to soil aridity in summer. This explains the saturation of integrated water vapor after 20°C observed by GPS and well captured by WRF (Figure 5). Figure 10c shows different behaviors for the 20th, 50th, and 80th. The upper percentile decreases with temperature from values which can reach 70% in winter and fall down to 25% in summer. The median percentile is fairly constant around 25% until 9°C. It increases up to 30% around 12°C and then decreases down to 17%. The 20th percentile does not show any trend and ranges between 7 and 15%. On average, Figure 12 shows that up to 15°C all terms of the budget increase with temperature, with a rate increasing between 9 and 15°C (water vapor convergence does not display a clear trend in general). There seems to be a compensation between the increase of precipitation rate and the water sources up to 9°C so the efficiency is rather constant. The precipitation term increases more sharply between 9°C and 12°C explaining the peak of  $\epsilon$ . For temperatures higher than 15°C, the precipitation term decreases at a higher rate than the hydrometeor and local water vapor change and hydrometeor convergence. Precipitation efficiency thus decreases with temperature as the result of enhanced rainfall evaporation in very dry environments during spring and summer [Frei and Schär, 1998]. In the updated Kain-Fritsch convective parameterization used in the WRF simulations, the closure is based on the convective available potential energy for an entraining parcel. This approach provides reasonable rainfall rates for a broad range of convective environments and it makes the updraft mass flux field a better predictor of convective intensity [Kain, 2004]. It has also been shown that Kain-Fritsch scheme gives results similar to those produced by cloud resolving model [Bechtold et al., 2001; Guichard et al., 2004; Hohenegger et al., 2009].



**Figure 13.** Schematic of the temperature–precipitation extremes relationship in the French Mediterranean region.

## 5. Discussion and Conclusion

Using the scaling of precipitation extremes with temperature at present to estimate precipitation trends in a warming climate is subject to caution. As also suggested by *Utsumi et al. [2011]*, using daily precipitation may lead to inaccurate conclusions as the Clausius–Clapeyron scaling may not predict daily precipitation extreme intensity increase with temperature. The potential applicability of the Clausius–Clapeyron scaling is improved at 3-hourly time scales in both the observations and simulations. However, even with 3-hourly precipitation data, the scaling at temperatures larger than 15°C can strongly deviate from Clausius–Clapeyron.

The variability of the scaling of precipitation extremes with temperature and its departure from thermodynamic Clausius–Clapeyron expectations can be related to various phenomena. The fact that surface temperature is used as a proxy for the temperature at condensation can lead to biases in arid situations, where water limitation is an issue. We believe that this is an important factor in the Mediterranean regions and will come back to that in the next paragraph.

Figure 13 is a schematic describing the processes explaining the scaling of precipitation extremes in the French Mediterranean region. Regime I (blue line) corresponds to winter and fall precipitation, which is mainly caused by large-scale perturbations. In the simulation, subgrid convective precipitation represents about 10% of the total precipitation until a temperature of about 15°C (not shown). In spring and summer, the contribution of large-scale precipitation drops to about 1–5% of the total (not shown). The transition between winter large-scale precipitation and summer convective precipitation occurs during spring following Regime II (green line). During this period, convective precipitation is associated with moderate vertical transport. Summer convective precipitation corresponds to Regime III (red line), with decreasing extreme values and dry conditions. Because of the dry environmental conditions, clouds and precipitation form at high levels so that the surface temperature used as a proxy for the temperature at condensation largely overestimates the actual temperature at condensation. The use of such a proxy at high temperatures in an arid environment partly causes the hook shape and the negative slope of the temperature–precipitation extremes curve at high temperatures.

Precipitation efficiency and vertical velocity in updrafts are also not necessarily constant with temperature. These can contribute to departures from CC scaling. In particular, the dry and arid conditions associated with the warmest temperatures (Regime III in Figure 13) yield lower precipitation efficiency. Fall precipitation is associated with either extreme “Cévenoles” events, strongly influenced by the orography (Regime IVb in Figure 13), and associated with a strong dynamic contribution (Figure 10b) or spring-like events (Regime IVa).

## References

- Allen, M. R., and W. J. Ingram (2002), Constraints on future changes in climate and the hydrological cycle, *Nature*, 419, 224–232.
- Alpert, P., et al. (2002), The paradoxical increase of Mediterranean extreme daily rainfall in spite of decrease in total values, *Geophys. Res. Lett.*, 29(11), 1536, doi:10.1029/2001GL013554.

## Acknowledgments

This work is a contribution to the HyMeX program (HYdrological cycle in the Mediterranean Experiment) through INSU-MISTRALS support and the MED-CORDEX program (COordinated Regional climate Downscaling Experiment—Mediterranean region). This research has received funding from the French National Research Agency (ANR) projects REMEMBER (contract ANR-12-SENV-001) and STARMP (contract ANR-12-JS06-0005). It was supported by the IPSL group for regional climate and environmental studies, with granted access to the HPC resources of IDRIS (under allocation i2011010227). The authors thank M. Stéfanon for performing the WRF simulations and O. Bock for providing IWV data retrieved from GPS. They acknowledge Météo-France for providing the surface weather station data ([donneespubliques.meteofrance.fr/](http://donneespubliques.meteofrance.fr/)) and teams of the HyMeX database ([mistrals.sedoo.fr/HyMeX/](http://mistrals.sedoo.fr/HyMeX/)) (ESPRI/IPSL and SEDOO/Observatoire Midi-Pyrénées) for their help in accessing the data. It is also a contribution to the cross-cutting activity on subdaily precipitation of the GEWEX program of the World Climate Research Program (WCRP) (GEWEX Hydroclimate Panel). B.A. and C.M. gratefully acknowledge financial support from the Chair for Sustainable Development at Ecole Polytechnique.

- Bastin, S., and P. Drobinski (2005), Temperature and wind velocity oscillations along a gentle slope during sea-breeze events, *Boundary Layer Meteorol.*, **114**, 573–594.
- Bastin, S., and P. Drobinski (2006), Sea breeze induced mass transport over complex terrain in southeastern France: A case study, *Q. J. R. Meteorol. Soc.*, **132**, 405–423.
- Bastin, S., C. Champollion, O. Bock, P. Drobinski, and F. Masson (2005), On the use of GPS tomography to investigate water vapor variability during a mistral/sea breeze event in Southeastern France, *Geophys. Res. Lett.*, **32**, L05808, doi:10.1029/2004GL021907.
- Bastin, S., C. Champollion, O. Bock, P. Drobinski, and F. Masson (2007), Diurnal cycle of water vapor as documented by a dense GPS network in a coastal area during ESCOMPTE-IOP2, *J. Appl. Meteorol. Climatol.*, **46**, 167–182.
- Bechtold, P., E. Bazile, F. Guichard, P. Mascart, and E. Richard (2001), A mass-flux convection scheme for regional and global models, *Q. J. R. Meteorol. Soc.*, **127**, 869–886.
- Berg, P., and J. O. Haerter (2013), Unexpected increase in precipitation intensity with temperature—A result of mixing precipitation types?, *Atmos. Res.*, **119**, 56–61.
- Berg, P., J. O. Haerter, P. Thejll, C. Piani, S. Hagemann, and J. H. Christensen (2009), Seasonal characteristics of the relationship between daily precipitation intensity and surface temperature, *J. Geophys. Res.*, **114**, D18102, doi:10.1029/2009JD012008.
- Berg, P., C. Moseley, and J. O. Haerter (2013), Strong increase in convective precipitation in response to higher temperatures, *Nat. Geosci.*, **6**, 181–185.
- Berthou, S., S. Mailler, P. Drobinski, T. Arsouze, S. Bastin, K. Béranger, and C. Lebeaupin-Brossier (2014), Prior history of Mistral and Tramontane winds modulates heavy precipitation events in Southern France, *Tellus*, **66**, 24064.
- Berthou, S., S. Mailler, P. Drobinski, T. Arsouze, S. Bastin, K. Béranger, and C. Lebeaupin-Brossier (2015), Sensitivity of an intense rain event between an atmosphere-only and an atmosphere-ocean coupled model: 19 September 1996, *Q. J. R. Meteorol. Soc.*, **141**, 258–271.
- Berthou, S., S. Mailler, P. Drobinski, T. Arsouze, S. Bastin, K. Béranger, E. Flaounas, C. Lebeaupin-Brossier, S. Somot, and M. Stéfanon (2016), Influence of submonthly air-sea coupling on heavy precipitation events in the Western Mediterranean basin, *Q. J. R. Meteorol. Soc.*, doi:10.1002/qj.2717, in press.
- Betts, A. K., and Harshvardhan (1987), Thermodynamic constraint on the cloud liquid water feedback in climate models, *J. Geophys. Res.*, **92**, 8483–8485.
- Braun, S. A. (2006), High-resolution simulation of Hurricane Bonnie 1998. Part II: Water budget, *J. Atmos. Sci.*, **63**, 43–64.
- Bresson, E., V. Ducrocq, O. Nuissier, D. Ricard, and C. de Saint-Aubin (2012), Idealized numerical simulations of quasi-stationary convective systems over the Northwestern Mediterranean complex terrain, *Q. J. R. Meteorol. Soc.*, **138**, 1751–1763.
- Bretherton, C. S., M. E. Peters, and L. E. Back (2004), Relationships between water vapor path and precipitation over the tropical oceans, *J. Clim.*, **17**, 1517–1528.
- Chen, C. T., and T. Knutson (2008), On the verification and comparison of extreme rainfall indices from climate models, *J. Clim.*, **21**, 1605–1621, doi:10.1002/2014GL060205.
- Chiriaco, M., S. Bastin, P. Yiou, M. Haeffelin, J.-C. Dupont, and M. Stéfanon (2014), European heatwave in July 2006: Observations and modeling showing how local processes amplify conducive large-scale conditions, *Geophys. Res. Lett.*, **41**, 5644–5652, doi:10.1002/2014GL060205.
- Crétat, J., B. Pohl, Y. Richard, and P. Drobinski (2012), Uncertainties in simulating regional climate of Southern Africa: Sensitivity to physical parameterizations using WRF, *Clim. Dyn.*, **38**, 613–634.
- Dee, D., et al. (2011), The ERA-Interim reanalysis: Configuration and performance of the data assimilation system, *Q. J. R. Meteorol. Soc.*, **137**, 553–597.
- Delrieu, G., et al. (2005), The catastrophic flash-flood event of 8–9 September 2002 in the Gard region, France: A first case study for the Cévennes-Vivarais Mediterranean hydrometeorological observatory, *J. Hydrometeorol.*, **6**, 34–52.
- Dequé, M., et al. (2005), Global high resolution versus limited area model scenarios over Europe: Results from the PRUDENCE project, *Clim. Dyn.*, **25**, 653–670.
- Di Luca, A., E. Flaounas, P. Drobinski, and C. Lebeaupin Brossier (2014), The atmospheric component of the Mediterranean Sea water budget in a WRF physics ensemble and observations, *Clim. Dyn.*, **43**, 2349–2375.
- Drobinski, P., et al. (2012), Modelling the Regional Coupled Earth system (MORCE): Application to process and climate studies in vulnerable regions, *Environ. Modell. Softw.*, **35**, 1–18.
- Drobinski, P., et al. (2014), HyMeX, a 10-year multidisciplinary program on the Mediterranean water cycle, *Bull. Am. Meteorol. Soc.*, **95**, 1063–1082.
- Ducrocq, V., D. Ricard, J. P. Lafore, and F. Orain (2002), Storm-scale numerical rainfall prediction for five precipitating events over France: On the importance of the initial humidity field, *Weather Forecasting*, **17**, 1236–1256.
- Ducrocq, V., O. Nuissier, D. Ricard, C. Lebeaupin, and T. Thouvenin (2008), A numerical study of three catastrophic precipitating events over southern France. Part II: Mesoscale triggering and stationarity factors, *Q. J. R. Meteorol. Soc.*, **134**, 131–145.
- Dudhia, J. (1989), Numerical study of convection observed during the winter monsoon experiment using a mesoscale two-dimensional model, *J. Atmos. Sci.*, **46**, 3077–3107.
- Durand, Y., E. Brun, L. Mérindol, G. Guyomarch, B. Lesaffre, and E. Martin (1993), A meteorological estimation of relevant parameters for snow models, *Ann. Glaciol.*, **18**, 65–71.
- Durand, Y., M. Laternser, G. Giraud, P. Etchevers, B. Lesaffre, and L. Mérindol (2009), Reanalysis of 44 years of climate in the French Alps (1958–2002): Methodology, model validation, climatology and trends for air temperature and precipitation, *J. Appl. Meteorol. Climatol.*, **48**, 429–449.
- Eggert, B., P. Berg, J. O. Haerter, D. Jacob, and C. Moseley (2015), Temporal and spatial scaling impacts on extreme precipitation, *Atmos. Chem. Phys.*, **15**, 5957–5971.
- Flaounas, E., P. Drobinski, M. Borga, J. C. Calvet, G. Delrieu, E. Morin, G. Tartari, and R. Toffolon (2012), Assessment of gridded observations used for climate model validation in the Mediterranean region: The HyMeX and MED-CORDEX framework, *Environ. Res. Lett.*, **7**, 024017, doi:10.1088/1748-9326/7/2/024017.
- Flaounas, E., P. Drobinski, M. Vrac, S. Bastin, C. Lebeaupin-Brossier, M. Stéfanon, M. Borga, and J. C. Calvet (2013), Precipitation and temperature space-time variability and extremes in the Mediterranean region: Evaluation of dynamical and statistical downscaling methods, *Clim. Dyn.*, **40**, 2687–2705.
- Flaounas, E., S. Raveh-Rubin, H. Wernli, P. Drobinski, and S. Bastin (2015), The dynamical structure of intense Mediterranean cyclones, *Clim. Dyn.*, **44**, 2411–2427.
- Frei, C., and C. Schär (1998), A precipitation climatology of the Alps from high-resolution rain-gauge observations, *Int. J. Climatol.*, **18**, 873–900.

- Gao, X., J. S. Pal, and F. Giorgi (2006), Projected changes in mean and extreme precipitation over the Mediterranean region from high resolution double nested RCM simulation, *Geophys. Res. Lett.*, 33, L03706, doi:10.1029/2005GL024954.
- Gibelin, A. L., and M. Déqué (2003), Anthropogenic climate change over the Mediterranean region simulated by a global variable resolution model, *Clim. Dyn.*, 20, 327–339.
- Giorgi, F. (2006), Climate change hot-spots, *Geophys. Res. Lett.*, 33, L08707, doi:10.1029/2006GL025734.
- Giorgi, F., and X. Bi (2005), Updated regional precipitation and temperature changes for the 21st century from ensembles of recent AOGCM simulations, *Geophys. Res. Lett.*, 32, L21715, doi:10.1029/2005GL024288.
- Guichard, F., et al. (2004), Modelling the diurnal cycle of deep precipitating convection over land with cloud-resolving models and single-column models, *Q. J. R. Meteorol. Soc.*, 130, 3139–3172.
- Haerter, J. O., and P. Berg (2009), Unexpected rise in extreme precipitation caused by a shift in rain type?, *Nat. Geosci.*, 2, 372–373.
- Haerter, J. O., P. Berg, and S. Hagemann (2010), Heavy rain intensity distributions on varying time scales and at different temperatures, *J. Geophys. Res.*, 115, D17102, doi:10.1029/2009JD013384.
- Hardwick Jones, R., S. Westra, and A. Sharma (2010), Observed relationships between extreme sub-daily precipitation, surface temperature, and relative humidity, *Geophys. Res. Lett.*, 37, L22805, doi:10.1029/2010GL045081.
- Held, I. M., and B. J. Soden (2006), Robust responses of the hydrological cycle to global warming, *J. Clim.*, 19, 5686–5699.
- Hohenegger, C., P. Brockhaus, C. S. Bretherton, and C. Schär (2009), The soil moisture-precipitation feedback in simulations with explicit and parameterized convection, *J. Clim.*, 22, 5003–5020.
- Hong, S. Y., J. Dudhia, and S. H. Chen (2004), A revised approach to ice microphysical processes for the bulk parameterization of clouds and precipitation, *Mon. Weather Rev.*, 132, 103–120.
- Holton, J. R., and G. J. Hakim (2013), *An Introduction to Dynamic Meteorology*, 532 pp., Academic Press, Amsterdam.
- Huang, H.-L., M.-J. Yang, and C.-H. Sui (2014), Water budget and precipitation efficiency of typhoon Morakot (2009), *J. Atmos. Sci.*, 71, 112–129.
- Kain, J. S. (2004), The Kain-Fritsch convective parameterization: An update, *J. Appl. Meteorol.*, 43, 170–181.
- Kharin, V. V., F. W. Zwiers, X. Zhang, and G. C. Hegerl (2007), Changes in temperature and precipitation extremes in the IPCC ensemble of global coupled model simulations, *J. Clim.*, 20, 1419–1444.
- Khodayar, S., G. Fosser, S. Berthou, S. Davolio, P. Drobinski, V. Ducrocq, R. Ferretti, M. Nuret, E. Pichelli, and E. Richard (2016), A seamless weather-climate multi-model intercomparison on the representation of high impact weather in the Western Mediterranean: HyMeX IOP12, *Q. J. R. Meteorol. Soc.*, doi:10.1002/qj.2700, in press.
- Köpen, W. (1936), Das geographische system der klimate, in *Handbuch der Klimatologie*, vol. 3, edited by C. W. Köpen and R. Geiger, pp. 1–46, Verlag von Gebrüder Borntraeger, Berlin.
- Lavaysse, C., M. Vrac, P. Drobinski, T. Vischel, and M. Lengaigne (2012), Statistical downscaling of the French Mediterranean climate: Assessment for present and projection in an anthropogenic scenario, *Nat. Hazards Earth Syst. Sci.*, 12, 651–670.
- Lebeaupin-Brossier, C., P. Drobinski, K. Béranger, S. Bastin, and F. Orain (2013), Ocean memory effect on the dynamics of coastal heavy precipitation preceded by a mistral event in the North-Western Mediterranean, *Q. J. R. Meteorol. Soc.*, 139, 1583–1597.
- Lebeaupin-Brossier, C., P. Drobinski, K. Béranger, and S. Bastin (2015), Regional mesoscale air-sea coupling impacts and extreme meteorological events role on the Mediterranean Sea water budget, *Clim. Dyn.*, 44, 1029–1051.
- Lebeaupin, C., V. Ducrocq, and H. Giordani (2006), Sensitivity of Mediterranean torrential rain events to the sea surface temperature based on high-resolution numerical forecasts, *J. Geophys. Res.*, 111, D12110, doi:10.1029/2005JD006541.
- Lenderink, G., and E. van Meijgaard (2008), Increase in hourly precipitation extremes beyond expectations from temperature changes, *Nat. Geosci.*, 1, 511–514.
- Lenderink, G., and E. van Meijgaard (2009), Unexpected rise in extreme precipitation caused by a shift in rain type? Reply to comment by Haerter et al, *Nat. Geosci.*, 2, 373.
- Lenderink, G., H. Y. Mok, T. C. Lee, and G. J. Van Oldenborgh (2011), Scaling and trends of hourly precipitation extremes in two different climate zones—Hong Kong and the Netherlands, *Hydrol. Earth Syst. Sci.*, 8, 4701–4719.
- Le Moigne, P. (2002), Description de l'analyse des champs de surface sur la France par le système SAFRAN (Description of the analysis of near-surface atmospheric fields over France with SAFRAN system) (in French), CNRM/GAME Rep., CNRM/GAME, Météo-France/CNRS, Toulouse, France.
- Meehl, G. A., et al. (2007), Global climate projections, in *Climate Change 2007: The Physical Science Basis. Contribution of Working Group I to the Fourth Assessment Report of the Intergovernmental Panel on Climate Change*, edited by S. Solomon et al., Cambridge Univ. Press, Cambridge, U. K., and New York.
- Min, S. K., X. Zhang, F. W. Zwiers, and G. C. Hegerl (2011), Human contribution to more-intense precipitation extremes, *Nature*, 470, 378–381.
- Mlawer, E. J., S. J. Taubman, P. D. Brown, M. J. Iacono, and S. A. Clough (1997), A validated correlated-k model for the longwave, *J. Geophys. Res.*, 102, 16,663–16,682.
- Moisselin, J. M., M. Schneider, C. Canellas, and O. Mestre (2002), Les changements climatiques en France au XX siècle: études des longues séries homogénéisées de données de température et de précipitations, *La Meteorol.*, 54, 33–42.
- Molnar, P., S. Fatici, L. Gaál, J. Szolgay, and P. Burlando (2015), Storm type effects on super Clausius-Clapeyron scaling of intense rainstorm properties with air temperature, *Hydrol. Earth Syst. Sci.*, 19, 1753–766.
- Muller, C. (2013), Impact of convective organization on the response of tropical precipitation extremes to warming, *J. Clim.*, 26, 5028–5043.
- Muller, C. J., P. A. O'Gorman, and L. E. Back (2011), Intensification of precipitation extremes with warming in a cloud resolving model, *J. Clim.*, 24, 2784–2800.
- Noh, Y., W. G. Cheon, S. Y. Hong, and S. Raasch (2003), Improvement of the k-profile model for the planetary boundary layer based on large eddy simulation data, *Boundary Layer Meteorol.*, 107, 401–427.
- O'Gorman, P. A. (2012), Sensitivity of tropical precipitation extremes to climate change, *Nat. Geosci.*, 5, 697–700.
- O'Gorman, P. A., and C. G. Muller (2010), How closely do changes in surface and column water vapour follow Clausius-Clapeyron scaling in climate change simulations, *Environ. Res. Lett.*, 5, 025207.
- O'Gorman, P. A., and T. Schneider (2009a), Scaling of precipitation extremes over a wide range of climates simulated with an idealized GCM, *J. Clim.*, 22, 5676–5685.
- O'Gorman, P. A., and T. Schneider (2009b), The physical basis for increases in precipitation extremes in simulations of 21st-century climate change, *Proc. Natl. Acad. Sci. U.S.A.*, 106, 14,773–14,777.
- Omran, H., P. Drobinski, and T. Dubois (2013), Optimal nudging strategies in regional climate modelling: Investigation in a Big-Brother Experiment over the European and Mediterranean regions, *Clim. Dyn.*, 41, 2451–2470.
- Omran, H., P. Drobinski, and T. Dubois (2015), Using nudging to improve global-regional dynamic consistency in limited-area climate modeling: What should we nudge?, *Clim. Dyn.*, 44, 1627–1644, doi:10.1007/s00382-014-2453-5.

- Oki, T., and S. Kanae (2006), Global hydrological cycles and world water resources, *Science*, **313**, 1068–1072.
- Pall, P., T. Aina, D. A. Stone, P. A. Stott, T. Nozawa, A. G. J. Hilberts, D. Lohmann, and M. R. Allen (2011), Anthropogenic greenhouse gas contribution to flood risk in England and Wales in autumn 2000, *Nature*, **470**, 382–385.
- Pall, P., M. R. Allen, and D. A. Stone (2007), Testing the Clausius-Clapeyron constraint on changes in extreme precipitation under CO<sub>2</sub> warming, *Clim. Dyn.*, **28**, 351–363.
- Panthou, G., A. Mailhot, E. Laurence, and G. Talbot (2014), Relationship between surface temperature and extreme rainfalls: A multi-timescale and event-based analysis, *J. Hydrometeorol.*, **15**, 1999–2011.
- Quereda Sala, J., A. Gil Olcina, A. Perez Cuevas, J. Olcina Cantos, A. Rico Amoros, and E. Montón Chiva (2000), Climatic warming in the Spanish Mediterranean: Natural trend or urban effect, *Clim. Change*, **46**, 473–483.
- Quintana-Seguí, P., P. Le Moigne, Y. Durand, E. Martin, F. Habets, M. Baillon, C. Canellas, L. Franchistéguy, and S. Morel (2008), Analysis of near surface atmospheric variables: Validation of the SAFRAN analysis over France, *J. Appl. Meteorol. Climatol.*, **47**, 92–107.
- Reale, M., and P. Lionello (2013), Synoptic climatology of winter intense precipitation events along the Mediterranean coasts, *Nat. Hazards Earth Syst. Sci.*, **13**, 1707–1722.
- Romps, D. M. (2011), Response of tropical precipitation to global warming, *J. Atmos. Sci.*, **68**, 123–138.
- Ruti, P., et al. (2015), MED-CORDEX initiative for Mediterranean climate studies, *Bull. Am. Meteorol. Soc.*, doi:10.1175/BAMS-D-14-00176.1.
- Salameh, T., P. Drobinski, and T. Dubos (2010), The effect of indiscriminate nudging time on the large and small scales in regional climate modelling: Application to the Mediterranean basin, *Q. J. R. Meteorol. Soc.*, **136**, 170–182.
- Singh, M. S., and P. A. O’Gorman (2012), Influence of microphysics on the scaling of precipitation extremes with temperature, *Geophys. Res. Lett.*, **41**, 6037–6044, doi:10.1002/2014GL061222.
- Singleton, A., and R. Toumi (2013), Super-Clausijs-Clapeyron scaling of rainfall in a model squall line, *Q. J. R. Meteorol. Soc.*, **139**, 334–339.
- Skamarock, W. C., J. B. Klemp, J. Dudhia, D. O. Gill, D. M. Barker, M. G. Duda, X. Y. Huang, W. Wang, and J. G. Powers (2008), A description of the advanced research WRF version 3, *Tech. Rep.*, NCAR, Boulder, Colo.
- Smirnova, T. G., J. M. Brown, and S. G. Benjamin (1997), Performance of different soil model configurations in simulating ground surface temperature and surface fluxes, *Mon. Weather Rev.*, **125**, 1870–1884.
- Solomon, S., et al. (2007), Technical summary, in *Climate Change 2007: The Physical Science Basis. Contribution of Working Group I to the Fourth Assessment Report of the Intergovernmental Panel on Climate Change*, edited by T. F. Stocker et al., Cambridge Univ. Press, Cambridge, U. K., and New York.
- Somot, S., F. Sevault, M. Déqué, and M. Crépon (2007), 21st century climate change scenario for the Mediterranean using a coupled atmosphere-ocean regional climate model, *Global Planet. Change*, **63**, 112–126.
- Stéfanon, M., F. D’Andrea, and P. Drobinski (2012), Heatwave classification over Europe and the Mediterranean region, *Env. Res. Lett.*, **7**, 014023, doi:10.1088/1748-9326/7/1/014023.
- Stéfanon, M., P. Drobinski, F. D’Andrea, C. Lebeaupin-Brossier, and S. Bastin (2014), Soil moisture-temperature feedbacks at meso-scale during heat waves over Western Europe, *Clim. Dyn.*, **42**, 1309–1324.
- Sugiyama, M., H. Shioigama, and S. Emori (2010), Precipitation extreme changes exceeding moisture content increases in MIROC and IPCC climate models, *Proc. Natl. Acad. Sci. U.S.A.*, **107**, 571–575.
- Sui, C. H., X. Li, M. J. Yang, and H. L. Huang (2005), Estimation of oceanic precipitation efficiency in cloud models, *J. Atmos. Sci.*, **62**, 4358–4370.
- Sui, C. H., X. Li, and M. J. Yang (2007), On the definition of precipitation efficiency, *J. Atmos. Sci.*, **64**, 4506–4513.
- Tarolli, P., M. Borga, E. Morin, and G. Delrieu (2012), Analysis of flash flood regimes in the North-Western and South-Eastern Mediterranean regions, *Nat. Hazards Earth Syst. Sci.*, **12**, 1255–1265.
- Trenberth, K. E., A. Dai, R. M. Rasmusson, and D. B. Parsons (2003), The changing character of precipitation, *Bull. Am. Meteorol. Soc.*, **84**, 1205–1217.
- Ulbrich, U., W. May, P. Lionello, J. G. Pinto, and S. Somot (2006), The Mediterranean climate change under global warming, in *Mediterranean Climate Variability*, edited by P. Lionello, P. Malanotte, and R. Boscolo, pp. 399–415, Elsevier, Amsterdam.
- Utsumi, N., S. Seto, S. Kanae, E. E. Maeda, and T. Oki (2011), Does higher surface temperature intensify extreme precipitation?, *Geophys. Res. Lett.*, **38**, L16708, doi:10.1029/2011GL048426.
- Vidal, J. P., E. Martin, L. Franchistéguy, M. Baillon, and J. M. Soubeyroux (2010), A 50-year high-resolution atmospheric reanalysis over France with the SAFRAN system, *Int. J. Climatol.*, **30**, 1627–1644.
- Vrac, M., P. Drobinski, A. Merlo, M. Herrmann, C. Lavaysse, L. Li, and S. Somot (2012), Dynamical and statistical downscaling of the French Mediterranean climate: Uncertainty assessment, *Nat. Hazards Earth Syst. Sci.*, **12**, 2769–2784.
- Westra, S., H. J. Fowler, J. P. Evans, L. V. Alexander, P. Berg, F. Johnson, E. J. Kendon, G. Lenderink, and N. M. Roberts (2014), Future changes to the intensity and frequency of short-duration extreme rainfall, *Rev. Geophys.*, **52**, 522–555, doi:10.1002/2014RG000464.
- Xoplaki, E., F. J. Gonzales-Rouco, J. Luterbacher, and H. Wanner (2003), Mediterranean summer air temperature variability and its connection to the large-scale atmospheric circulation and SSTs, *Clim. Dyn.*, **20**, 723–739.
- Xoplaki, E., F. J. Gonzales-Rouco, J. Luterbacher, and H. Wanner (2004), Wet season Mediterranean precipitation variability: Influence of large scale dynamics, *Clim. Dyn.*, **23**, 63–78.
- Yang, M. J., S. A. Braun, and D. S. Chen (2011), Water budget of Typhoon Nari (2001) at landfall, *Mon. Weather Rev.*, **139**, 3809–3828.
- Zhang, G. J. (2009), Effects of entrainment on convective available potential energy and closure assumptions in convection parameterization, *J. Geophys. Res.*, **114**, D07109, doi:10.1029/2008JD010976.